

**SIMULATION AND COMPARISON OF HIGH SPEED GAASSB-INP  
AND INGAAS-INP UNI-TRAVELING-CARRIER PHOTODIODES**

by

Ugur Guneroglu

A thesis submitted to the Faculty of the University of Delaware in partial fulfillment of the requirements for the degree of Master of Science in Electrical and Computer Engineering

Winter 2019

© 2019 Ugur Guneroglu  
All Rights Reserved

**SIMULATION AND COMPARISON OF HIGH SPEED GAASSB-INP  
AND INGAAS-INP UNI-TRAVELING-CARRIER PHOTODIODES**

by

Ugur Guneroglu

Approved: \_\_\_\_\_  
Yuping Zeng, Ph.D.  
Professor in charge of thesis on behalf of the Advisory Committee

Approved: \_\_\_\_\_  
Kenneth E. Barner, Ph. D.  
Chair of the Department of Electrical and Computer Engineering

Approved: \_\_\_\_\_  
Levi T. Thompson, Ph. D.  
Dean of the College of Engineering

Approved: \_\_\_\_\_  
Douglas J. Doren, Ph.D.  
Interim Vice Provost for Graduate & Professional Education

## **ACKNOWLEDGMENTS**

First, I would like to express my sincere gratitude to my adviser, Prof. Dr. Yuping Zeng, for her invaluable guidance, patience and support during the research. Without her help, I wouldn't be able to finish this project.

I would also like to thank the Turkish Ministry of Education for their amazing financial support and encouragement during my research.

I wish to thank my all group members for their help and sharing their ideas with me, especially' Kazy, Jie and all others. In this manner, special thanks to the Dun Mao who always helped me during the struggles that are related to the software

During my research, not everything went right, but nothing drove me to give up. In this point, I want to emphasize my appreciation to my beloved wife Ayse Sultan who always believed in me and supported me. This thesis is dedicated to her and my adorable, lovely daughter Meryem Hikmet who raised like sunshine to my life. Finally, I want to thank my dear mother, Hikmet and my father, Ahmet for their support and all other family members.

## TABLE OF CONTENTS

LIST OF TABLES .....	vi
LIST OF FIGURES .....	vii
ABSTRACT .....	ix

### Chapter

1	INTRODUCTION .....	1
2	WORKING PRINCIPLE, ADVANTAGES AND APPLICATIONS OF UTC-PD.....	3
2.1	Working principle and advantages of UTC-PD .....	3
2.2	Applications of UTC-PD.....	6
2.2.1	Wireless communication application .....	8
2.2.2	Spectroscopy application.....	9
2.2.3	Imaging Systems .....	11
3	THE SIMULATION SETUP .....	12
3.1	The Lumerical FDTD .....	12
3.1.1	The Solver Physics .....	13
3.1.2	Optical simulation setup details.....	16
3.1.2.1	Materials are used in the optical simulation .....	16
3.1.2.2	Building Up the Structure.....	21
3.1.2.3	Adding simulation region, selecting source and monitors.....	22
3.2	THE LUMERICAL DEVICE .....	27
3.2.1	The Solver Physics .....	28
3.2.2	Simulation Workflow .....	32
4	DESCRIPTION OF THE SIMULATION MODEL AND RESULTS .....	37
4.1	Simulation model's description.....	37

4.2	Results for GaAsSb/InP UTC-PD .....	39
4.3	Results for InGaAs/InP UTC-PD .....	44
	REFERENCES .....	49

## LIST OF TABLES

Table 2.1 Summary of UTC-PD's applications [4] .....	7
Table 3.1 The real and imaginary part of the refractive indices for the simulation materials for 1.3 $\mu\text{m}$ and 1.55 $\mu\text{m}$ wavelength .....	21
Table 4.1 Epitaxial layers of GaAsSb UTC-PD .....	38
Table 4.2 Epitaxial layers of InGaAs UTC-PD .....	39

## LIST OF FIGURES

Figure 2.1 Band diagram of UTC-PD (a) and pin-PD (b) [4] .....	4
Figure 2.2 Modified band diagram of UTC-PD (a) and pin-PD (b) [5] .....	6
Figure 2.3 The block diagram illustration of the wireless link system which is using UTC-PD in transmitter core [4].....	9
Figure 2.4 Using photonic MMW/THz wave generator in spectroscopy [4].....	10
Figure 2.5 Block diagram illustration of millimeter wave imaging system that using incoherent illumination. PC: Personal computer, SBD: Schottky-barrier diode [11].....	11
Figure 3.1 A Yee cell example [13] .....	14
Figure 3.2 Meshing in FDTD solver [13].....	15
Figure 3.3 Workflow for simulating photodetector [13].....	16
Figure 3.4 GaAsSb refractive index and absorption values over a wide range of wavelength [12] .....	18
Figure 3.5 Material Explorer window and data for GaAsSb.....	20
Figure 3.6 Structure's view in FDTD.....	22
Figure 3.7 Simulation region in FDTD .....	23
Figure 3.8 Example of Gaussian beam in FDTD .....	25
Figure 3.9 Frequency/Wavelength information about the source .....	26
Figure 3.10 Electric field in the source (a), Magnetic field in the source (b) .....	26
Figure 3.11 Illustration of mesh in Device.....	32
Figure 3.12 Global source shutter window on Device .....	34
Figure 3.13 Perspective view of the UTC-PD in Device .....	35

Figure 3.14 Perspective view of an active region in Device .....	36
Figure 4.1 Current-Voltage relation of GaAsSb/InP UTC-PD under dark and 1mW illumination for 1.3 $\mu\text{m}$ .....	40
Figure 4.2 Current-Voltage relation of GaAsSb/InP UTC-PD under dark and 1mW illumination for 1.55 $\mu\text{m}$ .....	40
Figure 4.3 Responsivity (A/W) in 1.3 $\mu\text{m}$ wavelength for GaAsSb/InP UTC-PD .....	41
Figure 4.4 Responsivity (A/W) in 1.55 $\mu\text{m}$ wavelength for GaAsSb/InP UTC-PD ....	42
Figure 4.5 3 dB cutoff frequency in 1.3 $\mu\text{m}$ wavelength for GaAsSb/InP UTC-PD $f_{3dB} = 66.4 \text{ GHz}$ .....	43
Figure 4.6 3 dB cutoff frequency in 1.55 $\mu\text{m}$ wavelength for GaAsSb/InP UTC-PD $f_{3dB} = 56.9 \text{ GHz}$ .....	44
Figure 4.7 IV curve for under dark and illumination for InGaAs/InP UTC-PD for 1.3 $\mu\text{m}$ .....	45
Figure 4.8 IV curve for under dark and illumination for InGaAs/InP UTC-PD for 1.55 $\mu\text{m}$ .....	46
Figure 4.9 Responsivity for InGaAs/InP UTC-PD for 1.3 $\mu\text{m}$ .....	47
Figure 4.10 Responsivity for InGaAs/InP UTC-PD for 1.55 $\mu\text{m}$ .....	47

## **ABSTRACT**

In this thesis, the performance of GaAsSb/InP and InGaAs/InP UTC-PD's are investigated by performing both optical and electrical simulations in Lumerical FDTD and Device software. Absorption material GaAsSb is replaced with InGaAs for the same reference structure. Voltage-current relation, responsivity as well as frequency response are obtained from the steady-state and transient simulations that are done for optical communication wavelengths which are 1.3  $\mu\text{m}$  and 1.55  $\mu\text{m}$ . Also, the systematics behind the simulation flow are presented.

## **Chapter 1**

### **INTRODUCTION**

The requirements on telecommunication technologies' area are rapidly growing since these technologies start to play an essential role in people's lives. Higher usage rate requires brings the need for using big data. Obviously, the higher data rate will necessitate higher speed telecommunication systems which must contain high speed electrical and optical components to cope with the data speed, especially in ultra-broadband wireless communication. In this manner, the importance of the generation of millimeter waves (30 GHz -10 THz) and/or terahertz (THz) waves is becoming more remarkable. This importance is not valid only for wireless communication, generation of millimeter waves is also a key for spectroscopic sensing as well as imaging. Naturally, these waves are very suitable for these kinds of applications. Photonic techniques are preferred over the electronic-based conventional techniques due to the stability, tunability and wide frequency bandwidth. In addition to the generation of millimeter waves, we are also able to distribute high-frequency RF signals by using fiber optic cables. In this manner, photodiodes' role starts to get more attention especially in optical (long wavelengths 1.3-1.55  $\mu\text{m}$ ). Plus, in this scheme, high output power is also important for large bandwidth applications. Various types of photodiode technologies for optical wavelengths are present to satisfy the needs. However, the uni-traveling-carrier photodiode and its variations have shown the highest output power between 100 GHz to 1 THz by getting enhanced in device structure and layers since it

was presented first in 1997 by Ishibashi (Ref [2]). The Ishibashi's model later numerically simulated in Ref [3] by Srivastava, [4], [5].

When it comes to UTC-PD's design, there are also two strong candidate materials for the active layer that is InGaAs and GaAsSb. Therefore, in this work, the performance of these two materials in the inspired design [1] are investigated. In Chapter 2, the basic working principle and advantages of UTC-PD are given as well as its applications. Chapter 3 focuses on giving details about the simulation software that are used for both optical and electrical simulations. Plus, the parameters such as refractive indices and absorption coefficients that are used in the optical simulation as well as its working principle are given in Chapter 3. Also, in terms of the electrical simulation, the models that are used by the software are highlighted. Finally, Chapter 4 is presenting the model's details that are used in this work and the results.

## Chapter 2

### WORKING PRINCIPLE, ADVANTAGES AND APPLICATIONS OF UTC-PD

#### 2.1 Working principle and advantages of UTC-PD

As its name implies, the uni-traveling-carrier photodetector uses only the electrons as the carriers which are the vital feature for appreciating its outstanding performance. The band diagrams of the UTC-PD and the traditional pin-PD are illustrated in Figure 2.1(a) and Figure 2.1(b) respectively. For an InGaAs pin-PD, absorption occurs in the depleted region (intrinsic layer) where electron-hole pairs are generated. On the other hand, there are two layers in UTC-PD's active region; one is the undepleted region narrow gap layer such as p-type InGaAs while the other one is undoped or lightly doped n-type depleted wide gap carrier collection layer. In the UTC-PD, the minority electrons that are generated by light absorption in the neutral absorption layer, first diffuse into the collection layer, then drift to the cathode layer. At the same time, photo-generated majority holes can respond very quickly in the dielectric relaxation time since the absorption layer is quasi-neutral. Thus, this effect causing, the dependence of UTC-PD's photoresponse on electron transport. In this point, the important difference shows up, between the UTC-PD and pin-PD which is the contribution of both holes and the electrons to the device's performance. Plus, the low-velocity hole transport is effective on complete device performance [4], [5].

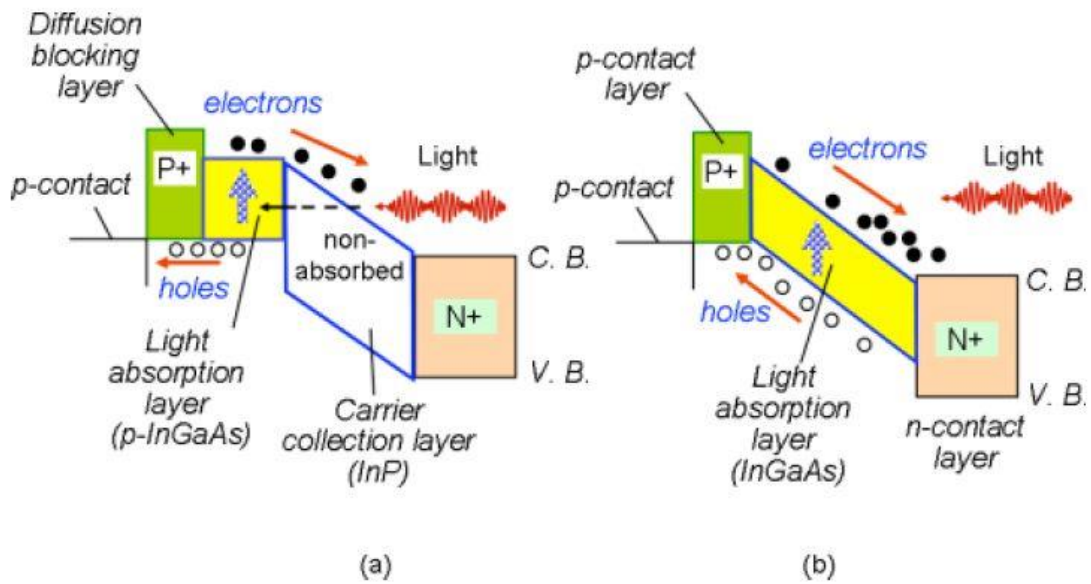


Figure 2.1 Band diagram of UTC-PD (a) and pin-PD (b) [4]

As shown in Figure 2.1 (a), when the light enters the photodetector, it is not really absorbed until it reaches the p-InGaAs absorption layer. It should be noted that, since there is no large electric field (nearly no electric field) in the absorption layer due to the heavy doping, the generated electrons and holes by absorption can diffuse in both directions. Since there is larger bandgap material on the left side of the absorption layer, conduction band discontinuity occurs and acts as a barrier to the electrons. Therefore, the electrons have no chance other than moving right side which towards to the collector layer. The collection layer is heavily doped with a high electric field that obtained by reverse biasing the detector. This layer drives all the electrons which can reach that the collection layer to the corresponding contact metal. [6]

UTC-PD has three significant advantages over conventional pin-PD. One advantage is having higher operation speed since the UTC-PD relies on electron transport rather than the holes. The electrons' velocity ( $3-5 \times 10^7$  cm/s) is approximately 10 times higher than the holes' velocity ( $5 \times 10^6$  cm/s). As mentioned previously, the

traditional pin-PD's operational speed is decided by the holes' speed while in UTC-PD's operation speed relies on the electrons' velocity. Therefore, the device's operation speed is determined by the electron diffusion time in the absorption layer in a proper UTC-PD design. Even the diffusion velocity can be considered less than the drift velocity under normal conditions, for a UTC-PD with thin absorption layer it is not the case. In this scheme, the diffusion velocity can be large because of the large minority mobility of electrons in p-InGaAs. [4], [5]

The second important advantage is high saturation output which is because of getting less affected from space charge effect in the depletion layer. When the conventional pin-PD is considered, it can be observed that the space charge density starts to increase according to increasing high-level light injection. In the condition of illuminating the device with a high level of light, the electric field starts to decrease since the mobile charges are gathered in the depletion region. The reduction on the electric field is causing the decrease of the carriers' velocity which means intensifying the space charge. It eventually, decreases the electric field more. Thus, this loop is named as space charge effect. Both pin-PD and UTC-PD are affected by the space charge effect. However, the UTC-PD is less affected. Pin-PD's band diagram is modified (band bending) because of the carrier's buildup under high excitation which can be seen in Figure 2.2 (b). Even for the reduced electric field, the velocity of the electrons is much higher than the holes, and in UTC-PD the space charge contains the electrons. This principle gives the advantage of having the output does not saturate up to moment where the current density turns out to higher than for the pin-PD. Additionally, in the pin-PD, when the current density is moderately low the holes' velocity starts to decrease. On the other hand, in the UTC-PD, the velocity of the

electrons does not begin to reduce until the electric field becomes much smaller. This phenomenon causes the UTC-PD has much wider linearity in comparison to pin-PD. [4], [5], [7]

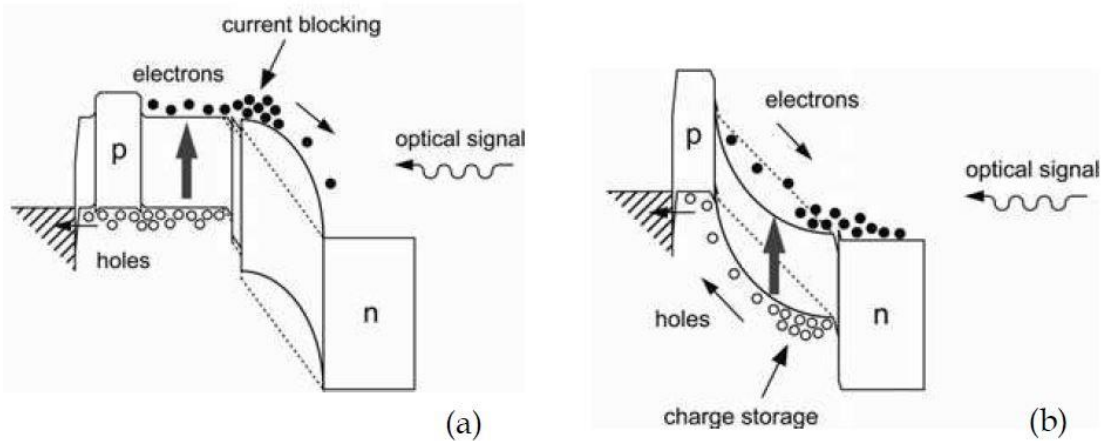


Figure 2.2 Modified band diagram of UTC-PD (a) and pin-PD (b) [5]

The capability of operating with low voltage is the third advantage of the UTC-PD. The high speed of the electrons can be preserved under a quite low electric field or even with a built-in electric field of the p-n junction itself. This situation causes the UTC-PD's high saturation output with high speed to be reserved with low voltage or zero voltage. However, in pin-PD high electric field necessitates maintaining the holes' drift speed. Obviously, the capability of operating at low voltage brings various advantages such as decreasing power consumption, simplifying the heat sinking, enhancing reliability and lastly decreasing biasing circuit cost. [4], [5]

## 2.2 Applications of UTC-PD

UTC-PD can find its place for several applications. Especially, Table 2.1 illustrates the areas of applications of a photonically produced millimeter and terahertz

waves. These are wireless communication, spectroscopy systems, and imaging systems. UTC-PDs are used in a different way for the applications mentioned. For instance, wireless systems are using the UTC-PDs to generate millimeter and sub-millimeter waves in the transmitter part of the system. In imaging systems, it can be benefitted from UTC-PDs by using them to generate noise signals photonically as an illuminator. Additionally, in the detector part of the spectroscopic measurement systems as mixers and also in the generator part.

Application	Generator	Detector
Communications	<b>Photonic emitter using UTC-PD</b>	Schottky-barrier Diode detector
Spectroscopy	<b>Photonic emitter using UTC-PD</b>	Schottky-barrier Diode detector
Active 1	<b>Photonic emitter using UTC-PD</b>	Diode detector
Active 2	<b>Photonic emitter using UTC-PD</b>	SIS mixer with <b>photonic LO</b>
Active 3	<b>Photonic emitter using UTC-PD</b>	<b>Photonic mixer using UTC-PD</b>
Passive	NA	SIS mixer with <b>photonic LO</b>
Imaging	<b>Photonic noise source using UTC-PD</b>	Schottky-barrier Diode detector

Table 2.1 Summary of UTC-PD's applications [4]

### **2.2.1 Wireless communication application**

120-GHz-band (with 125 GHz center frequency) wireless link system can be used as an example to illustrate the application of the UTC-PD in wireless systems. For example, the system with the ability to transmit data with a speed of 10 Gbit/s is shown by block diagrams in Figure 2.3. In the transmitter part of the system, a photonic millimeter-wave generator is employed. Subcarrier signals that are produced by the photonic-millimeter-wave generator are modulated at the center frequency which is 125 GHz. Mach-Zehnder modulator (MZM) is used to modulate the optical intensity (ASK) according to the data signal. Later, the high-power UTC-PD is fed by the output of the erbium-doped fiber amplifier (EDFA) which strengthens the subcarrier signal. The obtained optical signals are converted into millimeter wave signals by the UTC-PD. After this conversion, millimeter waves are also amplified by the HEMT amplifier before getting radiated via transmitter antenna. When the waves obtained by the receiver antenna, another amplification takes place before getting demodulated by using a basic envelope detection scheme, as an example. The receiver core includes pre-amplifier and Schottky-barrier diode which is based on InP-HEMT technology. [4], [5].

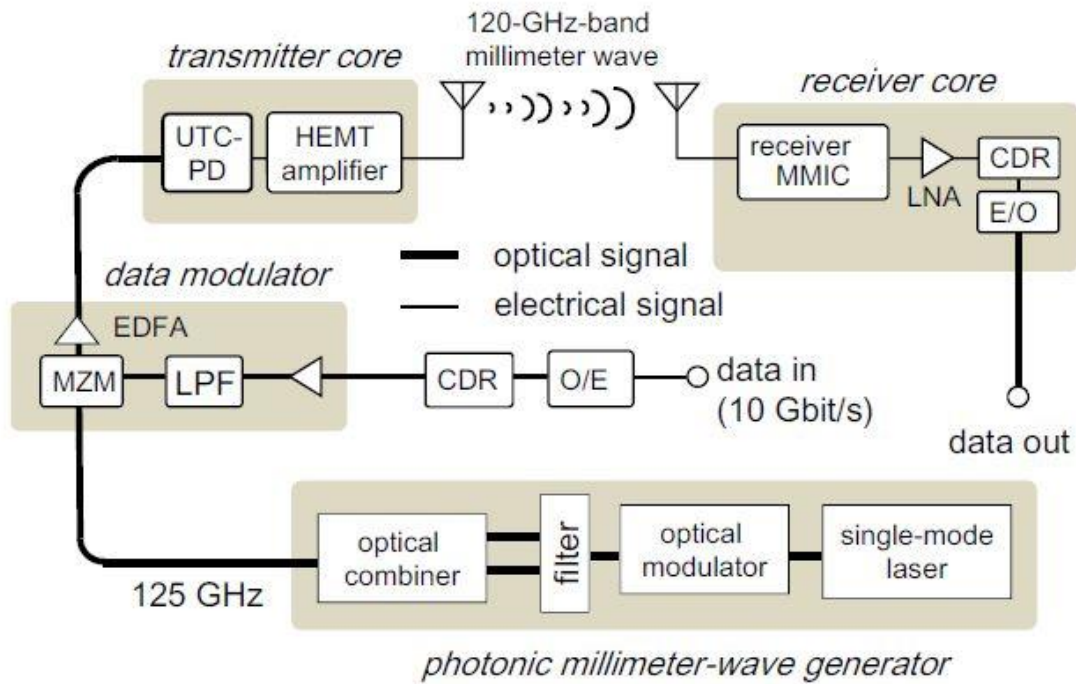


Figure 2.3 The block diagram illustration of the wireless link system which is using UTC-PD in transmitter core [4]

## 2.2.2 Spectroscopy application

THz waves have an important role such as interacting with matters, especially biological molecules such as proteins, DNA and chemicals. Another point to make is that also THz wave is useful to do material inspection and evaluation during and after manufacturing operation. Furthermore, the photonicly generated MMW/THz-wave signals have ultra-low noise characteristics which can be seen by their application to the LO for superconducting (SIS: superconductor-insulator-superconductor) mixers in heterodyne receivers, specifically in astronomy area. It is considered as the best combination to use photonic LO with SIS since the SIS needs very low LO power such as 10nW that is already obtained by using RF photodiodes. Additionally, photonic LO offers wide tunability in spectroscopy. Therefore, using low temperature operated UTC-

PD is making photonic LO more notable for mixing it with SIS. Figure 2.4 demonstrates the usage of the MMW/THz wave generator in the basic spectroscopic measurement system. In this system, the frequency is between 240 GHz and 360 GHz. A combination of  $N_2$  and  $NO_2$  with the ratio of 1:3. This combination is placed in a gas cell. The experimental setup is demonstrated in Figure 2.4. In order to sweep to the frequency and the optical MMW/THz signal, computer controlled MMW/THz signal generator is used. After that intensity modulation is used for the UTC-PD at 10 kHz frequency. Later, a diagonal horn antenna and off-axis parabolic mirror with gold coating are used to radiate and collimate the generated signal. Lastly, the generated signal is passing through the gas cell and received by the Schottky barrier diode and detected with lock-in amplifier adjusted frequency of 10 kHz [4], [5], [8], [9]

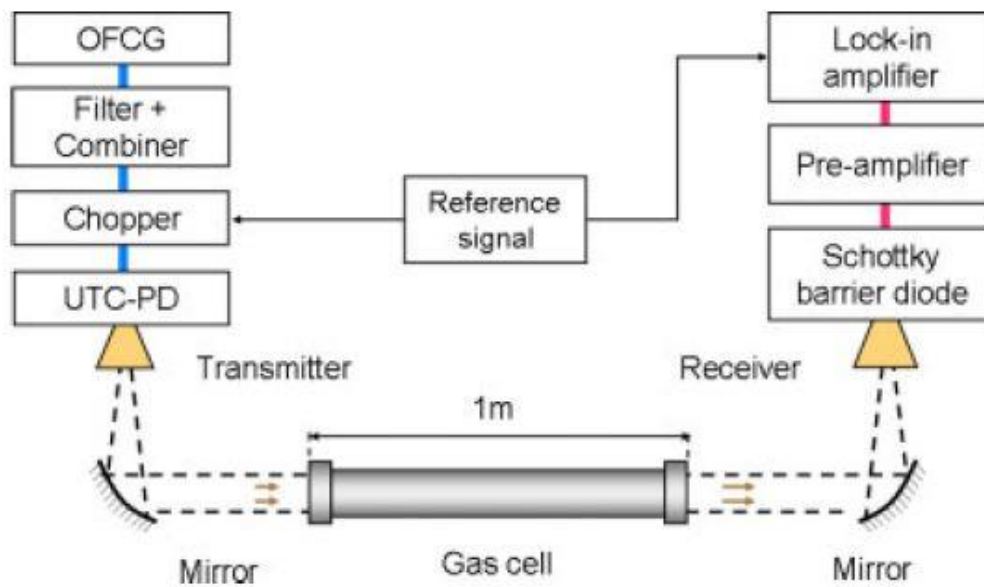


Figure 2.4 Using photonic MMW/THz wave generator in spectroscopy [4]

### 2.2.3 Imaging Systems

MMW/THz waves have been used widely in various areas such as security screening, quality control, and material inspection. Figure 2.5 shows the block diagram of a novel transmission-type imaging system which is using incoherent illumination from [11] as an example of using UTC-PD in imaging systems. Erbium-doped fiber amplifier (EDFA) is used to amplify spontaneous emission. Later the amplified spontaneous emission (ASE) is delivered to UTC-PD. The optical noise that received, later is converted to electrical noise via UTC-PD. Finally, a horn antenna is employed to radiate the electrical noise into free space. [4], [10], [11]

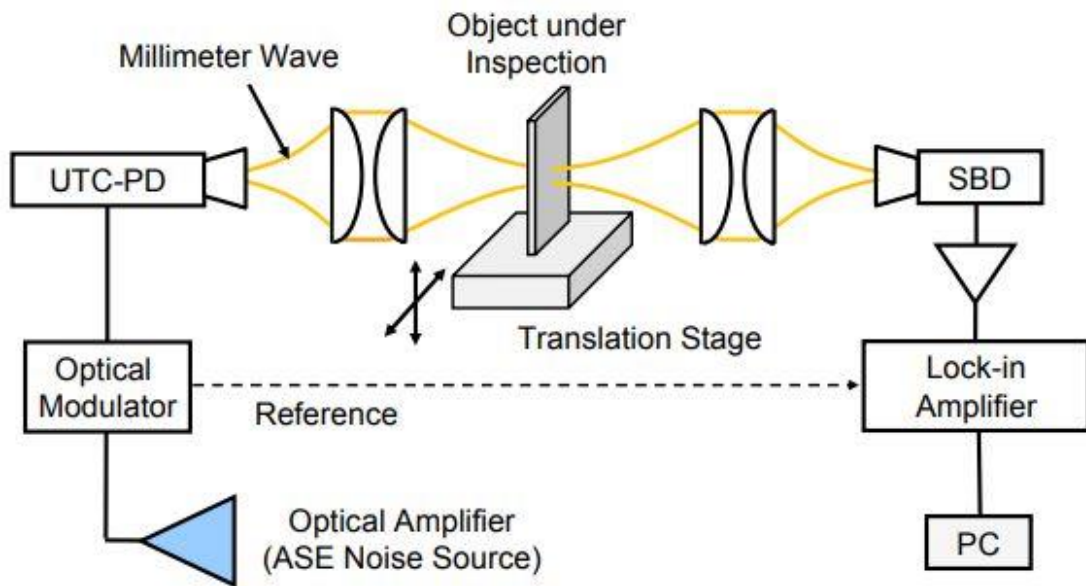


Figure 2.5 Block diagram illustration of millimeter wave imaging system that using incoherent illumination. PC: Personal computer, SBD: Schottky-barrier diode [11]

## Chapter 3

### THE SIMULATION SETUP

#### 3.1 The Lumerical FDTD

FDTD stands for Finite-Difference Time-Domain which is an advanced method for solving Maxwell's equations in sophisticated geometries. This method provides exceptional vision into problems that can be faced both in electromagnetics and photonics. The technique itself is advantageous when one prefers to simulate devices that feature sizes, smaller or at least on the order of the simulation wavelength. This is the point at which Snell's Law cannot answer the user's expectation which also means geometric optic (ray tracing method) does not work. The company Lumerical also named their powerful nanophotonic solver simulation software Lumerical FDTD which offers to solve Maxwell's equations both in 2D and 3D. In FDTD software, users can design components in wide range area of applications as well as active and passive integrated optics, plasmonics, nanoparticles, liquid crystals, defect detection, OLED/LED's, metamaterial, solar cells, CMOS image sensors, photonic crystals, and more. Moreover, there are useful quantities can be acquired such as complex pointing vector and transmission/reflection of the light by using FDTD. This is because FDTD can exploit Fourier transform solution to get frequency solutions. Therefore, FDTD is used to conduct optical simulation for UTC-PD to obtain electron-hole generation rate due to the absorption of the light [13].

### 3.1.1 The Solver Physics

It is convenient to briefly present the fundamental mathematical and physics structure behind the FDTD algorithm.

First, FDTD is capable of solving Maxwell's curl equations in non-magnetic materials

$$\frac{\partial \bar{D}}{\partial t} = \nabla \times \bar{H} \quad (3.1)$$

$$\bar{D}(\omega) = \varepsilon_0 \varepsilon_r(\omega) \bar{E}(\omega) \quad (3.2)$$

$$\frac{\partial \bar{H}}{\partial t} = -\frac{1}{\mu_0} \nabla \times \bar{E} \quad (3.3)$$

Where  $H$  represents the magnetic field,  $D$  displacement field, and  $E$  electric field.  $\varepsilon_r(\omega)$  symbolizing complex relative dielectric constant and it equals  $n^2$  while  $n$  is refractive index.  $E_x, E_y, E_z$  and  $H_x, H_y, H_z$  are the elements of Maxwell's equations in 3D.

Under the assumption of the structure is infinite in the z-direction, fields become independent from z, (3.4) and (3.5) shows that,

$$\varepsilon_r(\omega, x, y, z) = \varepsilon_r(\omega, x, y) \quad (3.4)$$

$$\frac{\partial \bar{E}}{\partial z} = \frac{\partial \bar{H}}{\partial z} = 0 \quad (3.5)$$

Then it causes to Maxwell's equation divided into two sets of equations which can be solved in the x-y plane and they are independent of each other's. These sets of equations are, TE:  $E_x, E_y, H_z$  and TM:  $H_x, H_y, E_z$ .

As an example, for TM (transverse magnetic), Maxwell's equations become;

$$\frac{\partial D_z}{\partial t} = \frac{\partial H_y}{\partial x} - \frac{\partial H_x}{\partial y} \quad (3.6)$$

$$D_z(\omega) = \varepsilon_0 \varepsilon_r(\omega) E_z(\omega) \quad (3.7)$$

$$\frac{\partial H_z}{\partial t} = -\frac{1}{\mu_0} \frac{\partial E_z}{\partial y} \quad (3.8)$$

$$\frac{\partial H_y}{\partial t} = -\frac{1}{\mu_0} \frac{\partial E_z}{\partial x} \quad (3.9)$$

These equations can be solved on a temporal grid, and discrete spatial by FDTD method and respectively every field component can be solved in a different position in Yee cell as shown in Figure 3.1.

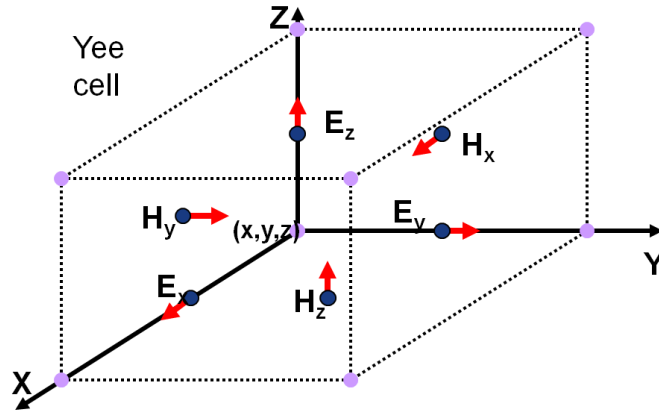


Figure 3.1 A Yee cell example [13]

For dispersive materials which have refractive index data (both real and imaginary parts) as a function of wavelength in a table, can be included in the multi-coefficient material model. This enables to software to generate data according to input (n, k) in the table or one can add (n, k) data for single wavelength as it is done in this thesis for the required materials, which is given in later in this chapter, in the optical simulation. Moreover, in the Lumerical FDTD solver, different light sources can be chosen such as guided mode, beams, dipole sources with different boundary conditions such as Bloch, periodic and PML. [13]

Cartesian style mesh is used in FDTD software as it is shown below in Figure 3.2. For more accurate results, a smaller mesh size can be used, but it will result in longer time with more memory requirement. In default, the mesh is automatically generated. Also, for the sake of the accuracy, FDTD Solver generates a smaller mesh in certain cases for instance, in the high index and highly absorbing materials to keep a constant number of mesh points per wavelength. Also, the Solver enables users to add mesh manually in case of need. [13]

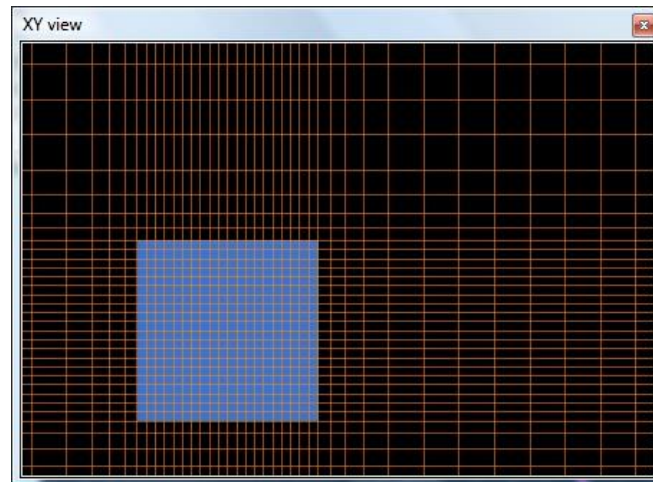


Figure 3.2 Meshing in FDTD solver [13]

The general workflow for simulating photodetector with Lumerical FDTD and Device solvers, the workflow needs to be followed is shown below in Figure 3.3. Even the default material library in FDTD is extensive; one may need to add material which is also done for this project. After adding the material, the desired device's structure geometry needs to be built up. Next, FDTD solver region where the user decides to use the desired boundary conditions, simulation time and mesh. Later, the required materials must be assigned to the related geometries. Following that the correct light

source and monitors should be chosen to both inject field and record data. In this project, the generation rate analysis object is also used to calculate electron-hole pairs due to the absorption of the light. The generation rate  $G(r)$  then is used as input to the Device software to calculate responsivity and frequency response. [13]

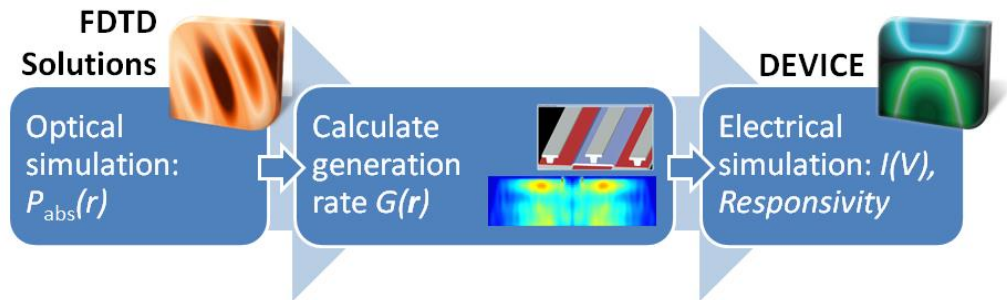


Figure 3.3 Workflow for simulating photodetector [13]

### 3.1.2 Optical simulation setup details

As mentioned previously, there are various options to select for sources, boundary conditions and materials to choose. To complete the simulation selecting the correct parameters and defining material is playing an essential role. The preferred setup conditions are given below.

#### 3.1.2.1 Materials used in the optical simulation

In the device which is the subject of this project has five different material used in it. These are Au, GaAsSb, InP, InGaAs, and AlGaAsSb. For Au and InP the FDTD solver's database is used. Other materials are added manually under (n, k) material model. FDTD solver offers different permittivity (or refractive index) material models such as (n, k) material model for single frequency simulation, Dielectric model that is

used produce material with constant refractive index , Sampled 3D (or 2D where the material can be defined by surface conductivity), which is used to import experimental data by text file, Conductive 3D model, Plasma (Drude) model, Debye model, Sell Meier model, Perfect Electrical Conductor (PEC) model which must have 100% reflection and 0% absorption and Analytic material model where user can define the real and imaginary part of the refractive index by defining equation. In (n, k) model user needs to put the n value which is the real part of the refractive index at the center frequency of the simulation which must be greater than zero. The k value is the imaginary part of the refractive index at the center of frequency of the simulation, and it can be either positive or negative value which sequentially corresponds to loss and gain. Since the simulation wavelength is 1.55  $\mu\text{m}$  (193.414 THz), the (n, k) data is collected from an external source according to the given operating frequency. After adding the material to the database, it is useful to check the fit from the material explorer window. Figure 3.5 demonstrates the GaAsSb index parameter information that is used in the simulation via material explorer window. The cross-section of the theoretical model and line 2 shows the real part and imaginary part of the refractive index which are put by the user. For broadband simulation, the user needs to add a table that contains the (n, k) data for the desired frequency range and can use the Sampled 3D model. The max coefficient and fit Tolerance values can be used to obtain a good fit for the simulation, for broadband simulation. [13]

Since GaAsSb is acting as an absorption layer, it plays a crucial role in the simulation to find out the device's performance. Specifically, reference [12], [18] and Lambert's law of absorption [14] are used to calculate the real and imaginary part of the

refractive index. Figure 3.4 illustrates GaAsSb's real part of the refractive index and absorption coefficient with lattice matching to InP. [12]

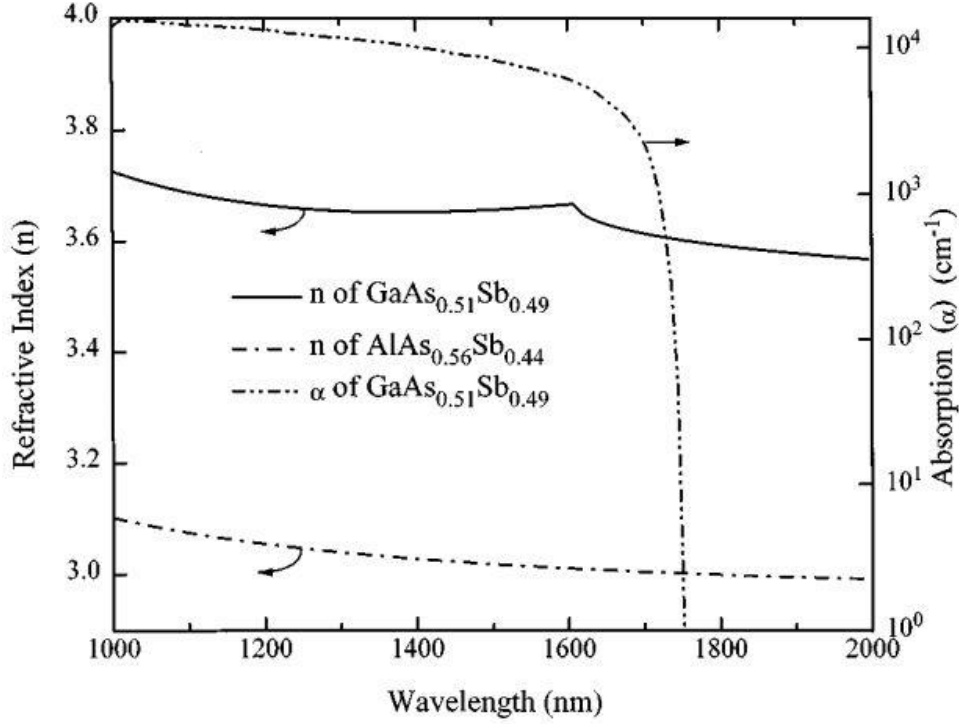


Figure 3.4 GaAsSb refractive index and absorption values over a wide range of wavelength [12]

Considering a plane wave with  $f$  frequency propagates through a solid and its velocity  $v$  while traveling in the  $x$ -direction, then the electric field can be defined as following equation (3.10)

$$E = E_0 \exp\{i2\pi f [t - (x/v)]\} \quad (3.10)$$

While  $E_0$  shows incident field and  $\{i2\pi f [t - (x/v)]\}$  is the displacement at time  $t$ . Maxwell's equations indicate that the speed of light  $c$  has a relation with the permittivity of the free space  $\epsilon_0$  and the permeability of free space  $\mu_0$ . The equation (3.11) shows this relation

$$c = \frac{1}{\sqrt{\mu_0 \epsilon_0}} \quad (3.11)$$

The relation of the speed of light in a vacuum ( $c = f\lambda$ ) and the solid's complex refractive index is  $N = n - ik$  which is defined by (3.12)

$$\frac{1}{v} = \frac{n}{c} - \frac{ik}{c} \quad (3.12)$$

By substituting (3.12) in (3.10) gives the following equation (3.13)

$$E = E_0 \exp(i2\pi ft) \exp\left(\frac{-i2\pi xn}{c}\right) \exp\left(\frac{-i2\pi f k x}{c}\right) \quad (3.13)$$

Where the last term  $-i2\pi f k x/c$  represents the measure of the extinction coefficient ( $k$ ). Square of electric field vector multiplied by conductivity  $\sigma$  gives the power of the electric field which is also the intensity of the light is provided by (3.14).

$$(P = \sigma \times E^2) \quad (3.14)$$

After using the extinction coefficient term, the following equation which shows the fraction of the power of the traveling wave from location 0 to  $x$  can be obtained

$$\frac{P(x)}{P(0)} = \frac{\sigma E^2(x)}{\sigma E^2(0)} = \exp\left(\frac{-4\pi f k x}{c}\right) \quad (3.15)$$

This leads to obtaining the equation the absorption coefficient  $\alpha$  can be obtained by using extinction coefficient  $k$

$$\alpha = \frac{4\pi f k}{c} \quad (3.16)$$

Then, (3.15) can be expressed as  $P(x) = P(0)e^{\alpha x}$  which is known as Lambert's law (or Bouguer's law). Consequently, from the equations and expressions above, it is shown that the thickness, characteristics of the medium and the radiation wavelength have a strong impact on the absorbed radiation to an extent. From Figure 3.4 the real part of the refractive index can be found as 3.64 for the desired wavelength of 1550 nm. To find the imaginary part of the refractive index, the absorption coefficient value need be gotten. Thus, from Figure 3.4, the value for absorption coefficient can be read as approximately  $6800 \text{ cm}^{-1}$  while also [18] giving the exact value for the 1550 nm wavelength. Using this value in equation (3.16 leads us to find  $k$  value as 0.084 for 1550 nm. These values are used for GaAsSb in the optical simulation. Figure 3.5 also shows the calculated and used values in material explorer which is a useful tool to check materials' fit before running the simulation

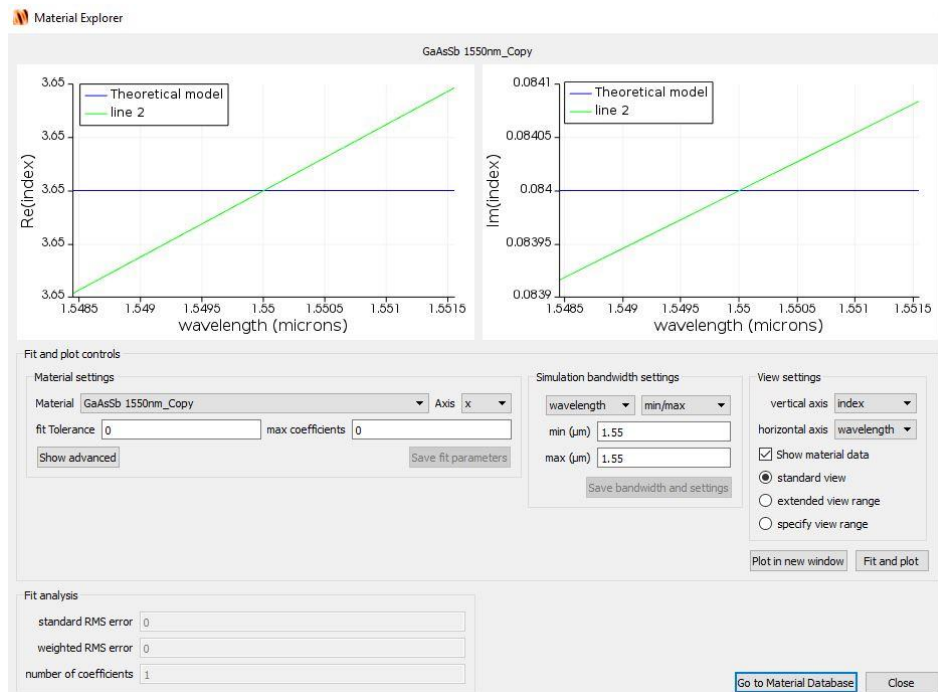


Figure 3.5 Material Explorer window and data for GaAsSb

For rest of the materials that are not in the FDTD solver's database such as AlGaAsSb and InGaAs, the real and imaginary part of refractive index are obtained and calculated from related sources given in table 3.1.

Table 3.1 The real and imaginary part of the refractive indices for the simulation materials for 1.3  $\mu\text{m}$  and 1.55  $\mu\text{m}$  wavelength.

Material	$n(1.3\mu\text{m})$	$k(1.3\mu\text{m})$	$n(1.55\mu\text{m})$	$k(1.55\mu\text{m})$
Au	0.408	8.305	0.559	9.81
InP	3.2	0	3.167	0
GaAsSb	3.64 [12]	0.093 [18]	3.65 [12]	0.084 [12], [18]
InGaAs	3.45 [19]	0.12 [19], [22], [23]	3.58 [19]	0.080 [19], [20], [21]
AlGaAsSb	3.96 [16]	0	3.79 [16]	0

### 3.1.2.2 Building Up the Structure

After setting up materials' data, the photodetector's structure geometry needs to be built up. To achieve this purpose, one can select the desired object such as a triangle, rectangular, polygon, surface, custom and so on. Next, the structure can be edited from its window by defining the geometry (coordinates), assigning the material to the object and even can change the object's graphical rendering to make it transparent (regarding visualization). Changing graphical rendering helps to see other layers through the layer that its graphical render's value decreased such as buried structures. Figure 3.6 shows the x-y, x-z, y-z and perspective view of the structure under the FDTD solver window. It is also possible to add structure by using the script. It can be noted that Lumerical has its scripting language which is partially similar to MATLAB.

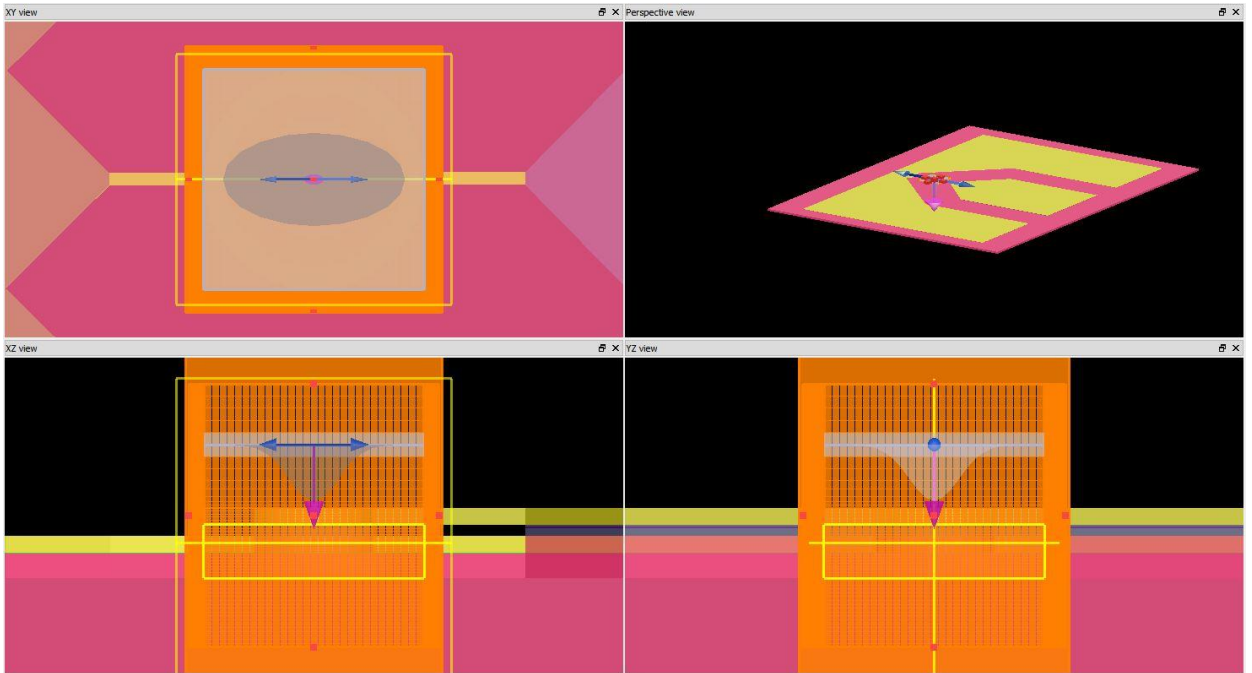


Figure 3.6 Structure's view in FDTD

FDTD also allows users to add more complex geometries by importing them from CAD in GDSII, or STL format. The user can use images or surface height data over the position to import the desired structure. Correspondingly, object library, which has a good amount of variety of prebuilt structures, can be used for adding an object.

### 3.1.2.3 Adding simulation region, selecting source and monitors

Setting up the structure's objects are followed by adding the FDTD simulation region. This is where the user can decide simulation parameters such as simulation time, temperature, dimension, mesh settings, and boundary conditions. Starting with FDTD simulation region base properties; dimension is set up to 3D, background index is set up one which is background medium's refractive index and simulation time is 1000 fs. It is useful to point out that the simulation time refers to the maximum time of the

simulation to be completed. However, the simulation may end earlier if the auto shutoff criteria are satisfied before the maximum simulation time is reached. Under the simulation region tab, the geometry of the simulation region needs to be determined. Figure 3.7 shows the perspective view of the simulation region which is 3D rectangular with orange lines. As is seen, it is surrounding the whole active area of the device.

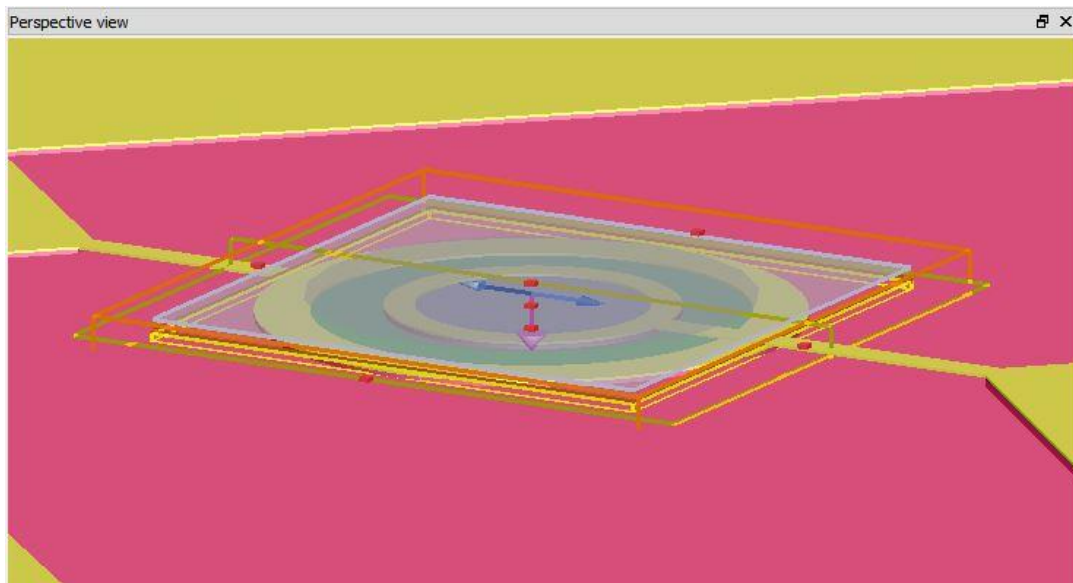


Figure 3.7 Simulation region in FDTD

For mesh settings, the auto non-uniform mesh is selected among the custom non-uniform and uniform algorithm options with dt stability factor 0.99 which determines the size of the time step used during the simulation which is defined as a fraction of Courant stability factor and  $dt(fs)$  is 0.035344. FDTD solver also supports different types of boundary conditions such as PML (Perfectly Matched Layer), metal, PMC (Perfect Magnetic Conductor), periodic, Bloch, symmetric and antisymmetric boundary conditions. PML boundaries can absorb the electromagnetic waves incident on their surface which means there is no reflection upon them when these boundaries are used.

Under the simulation tab, there are parameters that allow the user to control absorption specifications. Metal boundaries act as a perfect electrical conductor (PEC) while PMC is the magnetic equivalent of PEC. Periodic boundaries are useful when both the structure and the electromagnetic fields are periodic. Bloch boundary conditions also are similar to periodic boundaries except Bloch boundaries are helpful when there is a phase shift between the fields. Symmetric boundaries can be used when there is one or more symmetric geometry is used in the structure. Source also must be symmetric to get logical results. This acts as a mirror for the field. Opposite conditions are valid for the antisymmetric boundaries. In this simulation, PML boundaries are used to prevent reflection. [13]

There are also several optical source types available in FDTD solver. Such as; point (dipole) sources which act as a source in Maxwell's equation to produce fields. Total-field scattered-field sources are useful when one needs to separate the computation region into two distinct regions while one of the regions just contain scattered field and the other has only the total field. Plane wave sources can be used to inject laterally uniform radiation from one side of the source. If desired, also mode sources can be selected to insert guided mode. The user also can import his source by deciding a custom profile for the source. Global source options set the default frequency parameters. Last, there is also Gaussian and Cauchy\ Lorentzian sources which are used in this project. This type allows us to define electromagnetic radiation with the amplitude defined by Gaussian cross-section of a given width and propagating in a certain path. In default option, Gaussian source uses scalar beam approximation for the electric field that is effectual while the beam waist parameter is larger than the

diffraction limit. Also, this approach accepts that the field in the direction of the propagation is zero. Figure 3.8 shows an illustration of a Gaussian beam in FDTD. [13]

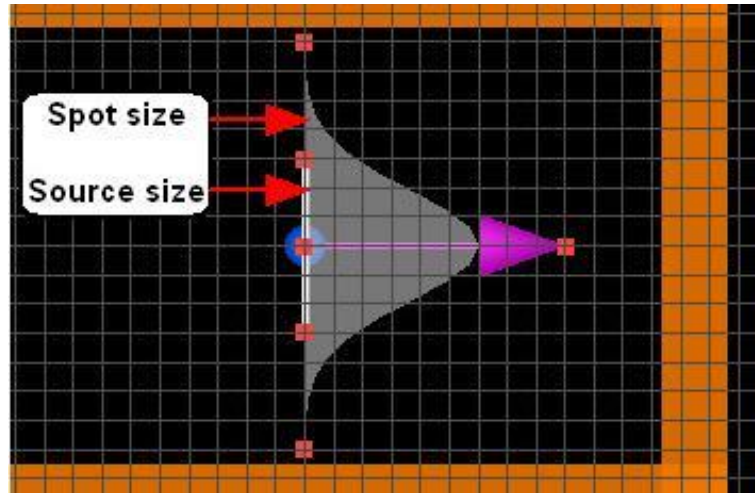


Figure 3.8 Example of Gaussian beam in FDTD

The parameters for the source that is used in this project are given below. Plus, electric and magnetic fields are also shown. These figures are obtained after setting up the beam data by visualizing it.

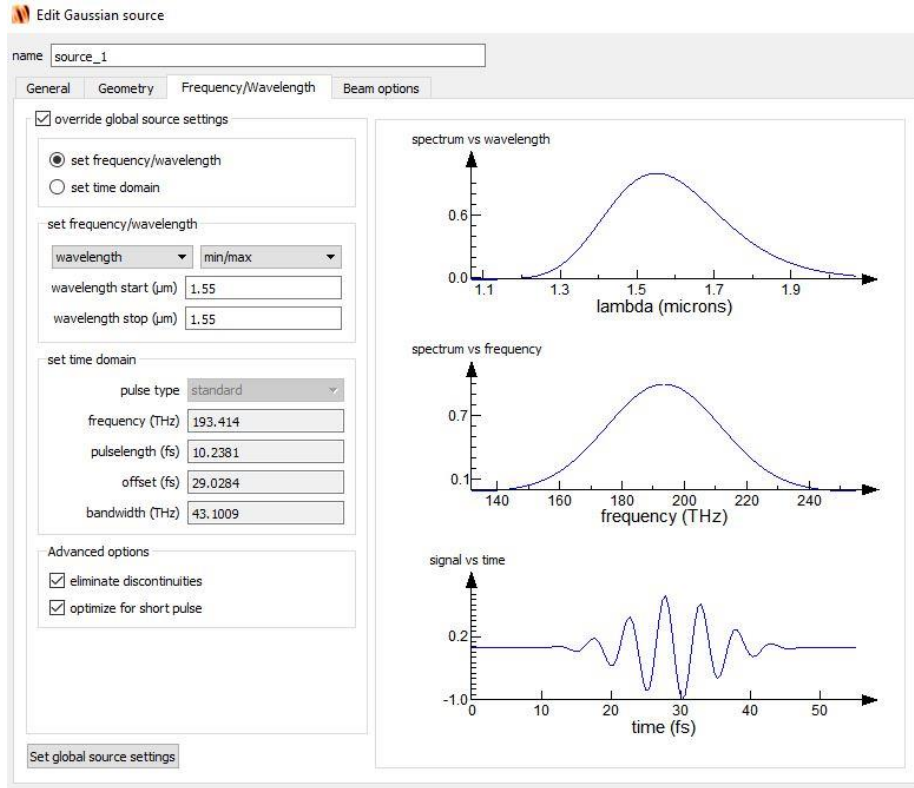


Figure 3.9 Frequency/Wavelength information about the source

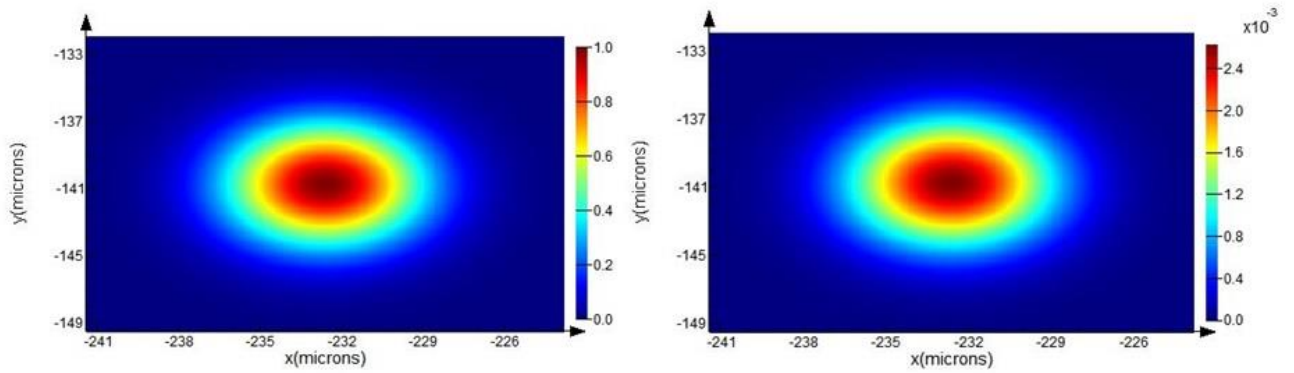


Figure 3.10 Electric field in the source (a), Magnetic field in the source (b)

To obtain the data for electron-hole pairs that are generated under the illumination, generation rate object is used from analysis group. Generation rate can also be calculated from (3.17) given below,

$$G = \eta_0 \frac{P^* \lambda}{hc} \alpha e^{-\alpha y} \quad (3.17)$$

Where  $P^*$  is optical power,  $\eta_0$  is internal quantum efficiency,  $\lambda$  is wavelength,  $h$  is Planck constant,  $c$  is the speed of the light,  $\alpha$  is absorption coefficient and  $y$  is the distance from the surface. [24]

As explained before, the calculated photogeneration rate is lately imported to the Device to calculate the current under illumination, responsivity and frequency response. Also, index monitor is used to recording  $n$  and  $k$  value as a function frequency. Additionally, frequency-domain field monitors are used to obtaining CW and steady-state electromagnetic field data in the simulation.

### **3.2 THE LUMERICAL DEVICE**

Lumerical Device software is an extraordinary tool for both electrical and thermal simulations semiconductors and optoelectronic components. It is pronounced as the world's first multiphysics simulation suite purpose-built for photonic designers, by photonic designers. It includes several solvers that users can choose. Such as, the Device Heat Transport Solver which provides inclusive thermal modeling capability, efficiently handling conductive, convective, and radiative effects, while also gives the heat due to the electrical and optical effects. Another solver is the Finite Device Element Eigen Mode Solver which is used to investigate waveguide modes while geometries and material properties are present. The other solver is named the Device

Discontinuous Galerkin Time Domain Solver which works even complex geometries. Lastly, the Device Charge Solver which is used in this project, built on the finite element drift-diffusion method and offers comprehensive charge transport analyze. In the next section, the physic behind the solver is given. [13]

### 3.2.1 The Solver Physics

The basic physic behind the Device software algorithm is given by beginning from the non-linear Poisson and drift-diffusion equations. The Device is proficient to solve the drift-diffusion equations for carriers (both electrons and holes),

$$\mathbf{J}_n = q\mu_n n\mathbf{E} + qD_n \nabla n \quad (3.18)$$

$$\mathbf{J}_p = q\mu_p p\mathbf{E} + qD_p \nabla p \quad (3.19)$$

Where the  $\mathbf{J}_{n,p}$  is the current density,  $q$  is the positive electron charge,  $\mu_{n,p}$  is the mobility,  $D_{n,p}$  is the diffusivity,  $\mathbf{E}$  is the electric field and  $n$  and  $p$  are the electrons and holes densities. There is two main process that causes each of the electrons and holes movement in the material. One of these processes is the drift due to the electric field while the other one is the random thermal diffusion due to the gradient in the density. The drift diffusion equations illustrate these two processes as a summation of the two terms.

It is also beneficial to point out that the mobility defines the ease of the movement of the carriers through the semiconductor. There is a connection between the diffusivity  $D_{n,p}$  and the mobility  $\mu_{n,p}$  by the Einstein relation,

$$D_{n,p} = \mu_{n,p} \frac{k_B T}{q} \quad (3.20)$$

$k_B$  Is the Boltzmann constant. It is possible to model the mobility, which is a crucial parameter, as a function of the temperature, carrier concentration, doping concentration, and the electric field.

To solve the drift-diffusion equations, it is necessary to find the electric field first. Poisson's equation can be solved to find out the electric field,

$$-\nabla \cdot (\epsilon \nabla V) = q\rho \quad (3.21)$$

where  $V$  is the electrostatic potential,  $\epsilon$  is the dielectric permittivity and  $\rho$  is the net charge density,

$$\rho = p - n + C \quad (3.22)$$

and  $C$  stands for the contribution which is coming from the ionized impurity density.

Also, it is essential to consider the auxiliary continuity equations for the charge conservation,

$$\frac{\partial n}{\partial t} = \frac{1}{q} \nabla \cdot \mathbf{J}_n - R_n \quad (3.23)$$

$$\frac{\partial p}{\partial t} = \frac{1}{q} \nabla \cdot \mathbf{J}_p - R_p \quad (3.24)$$

where the  $R_{n,p}$  is the difference between the recombination rate and generation rate (net recombination rate). The consequence of the physical processes, which is related to the material, are expected to behave equally and give,  $R = R_n = R_p$ . It is worth highlighting that the generation and recombination processes are vital factors in the material specific calculation of carrier behavior. One can find different type models of the generation and

recombination processes in the Device based on temperature, doping concentration, electric field, and current density.

The Poisson's and drift-diffusion equations are discretized and solved by the Device software on unstructured finite-element mesh both in one and two dimensions. There are multiple categories of materials in the Device such as insulators, conductors and semiconductors while each of the material has a user-specified model or collection of models that define its performance.

The equations solved by the Device accept both time-varying and steady state results. By applying the condition,

$$\frac{\partial n}{\partial t} = \frac{\partial p}{\partial t} = 0 \quad (3.25)$$

in the continuity equations, the electrostatic potential and the carrier density can also be solved at steady-state simulation which is used to examine the system's behavior at a fixed operating point.

It is essential to emphasize the importance of boundary conditions in an accurate device simulation. One of the boundary condition types is related to the electrostatic potential (Poisson's equation) while the other one is linked to the carrier densities (the drift-diffusion equations). Since the Poisson's and drift-diffusion equations are second-order partial differential equations which cause that each of them necessitates that the solution is clearly specified for at least one location. This phenomenon is identified as a Dirichlet boundary condition. The Dirichlet condition gets the form of the internal or external boundary with a constant voltage for the electrostatic potential,

$$V(x) = V_1 \quad (3.26)$$

which is an example of electrical contact. At the interface between the semiconductor and the contact, the carrier concentration is specified to its equilibrium value as shown below

$$p-n+C=0 \quad (3.27)$$

The physical properties of the interface play an important role when the boundary conditions are needing to be determined at internal boundaries. The electric flux density must be continuous through the boundary when the surface charges are not present for the case of electrostatic potential. It is probable to specify boundary conditions between the semiconductor and adjacent materials regarding surface recombination current density or an infinite recombination velocity (for contacts) for the electron and hole densities. Surface recombination current density is defined zero in default which means no carrier flux through the boundary

Homogenous Neumann boundary conditions are applied at the external boundaries of the simulation domain. The electric field normal to the boundary is arranged to be zero just as the surface current density. This situation physically accounts for insulating boundary across that no charge can flow. The device also using an unstructured, finite-element mesh which can be seen in Figure 3.11. To find the physical quantities of the related material, the solution of the system of equations needs to be used while an estimation is also needing to be performed from the discrete formulation of those equations. Thus, the importance of the understanding of the necessary simulation quantities such as, material properties, electrostatic potential, carrier concentration and geometry information which are calculated at each mesh vertex, must be emphasized.

As it is mentioned in FDTD, also in Device, using a finer mesh which means shorter edge lengths and smaller element, reasons of needing more memory and simulation time. [13]

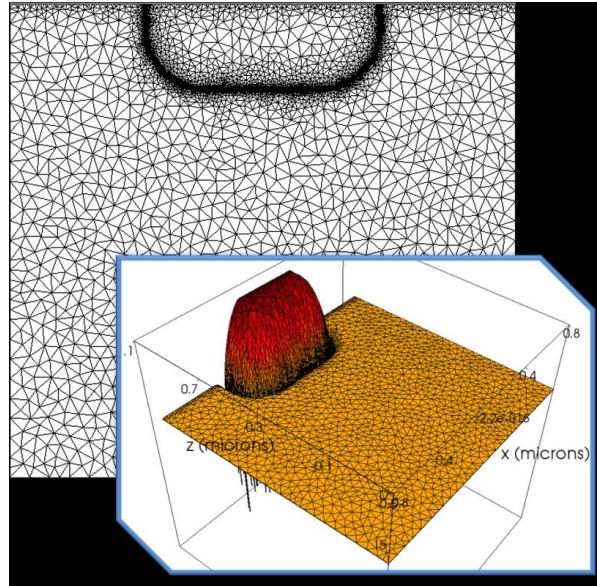


Figure 3.11 Illustration of mesh in Device

### 3.2.2 Simulation Workflow

Simulation workflow in Device is quite similar to FDTD. It is essential to mention the steps to design and simulate the device. There are five important steps in the workflow which must be followed carefully. The first step is specifying the materials that are going to be used in the simulation. Therefore, one needs to make the material list that is going to be used in the simulation and assign optical, electrical and thermal properties. In default, Device has a variety of materials in its library, and it also allows you to add material (in semiconductor, binary alloy, insulator, conductor, and fluid categories). Since AlGaAsSb cannot be found in the library, it is added by the user

by combining AlGaAs with GaSb. Since optical simulation done in FDTD, it is not necessary to add optical or thermal properties of the material for this project since we are just interested in the electrical behavior of the device. The second step is defining or importing your geometric objects set up desired device's structure followed by assigning the materials that are listed to the geometric objects. As soon as assign the materials, solver regions and monitors must be added which is the third step in the workflow. In this manner, charge solver added with charge and band monitor to collect data from the device. As a fourth step, the designer needs to define solver specific objects to the simulation, such as boundary conditions, monitors and sources. Plus, the partitioned volume enables to be sure if the solver(s) placed as intended. The last step is checking the error and analyzing the results. It is also important to point out that there are two solver types under charge solver advanced tab. These are Newton and Gummel solvers where they have weak and powerful points. The user needs to choose the correct solver for the simulation. As an example, the Gummel solver is faster than the Newton solver in numerical aspect. However, the reliability of this solver turns out to be less when the current that is flowing in the device is large. That is the reason for choosing Gummel solver in reverse bias while Newton solver is used in forwarding bias. For transient simulations also, Newton solver must be selected. In the advanced tab of charge solver, there is an option to choose between Fermi and Boltzmann statistics which describes the charge distribution in the semiconductor. It is easier for the solver to calculate charge density in the Boltzmann model. However, the device needs to be undoped or lightly doped. When the high doping is used, the Boltzmann statistics becomes invalid, and the user must choose Fermis statistics which is also preferred in

this simulation. Additionally, the output of the FDTD which is the generation rate is imported to Device. [13]

To find dark current (both under reverse and forward bias), the imported generation rate object must be disabled first. Then voltage must be swept on the electrical contact. After finding the dark current, generation rate is enabled to find responsivity (A/W). The last step of characterizing of the UTC-PD is calculating the bandwidth. To achieve this purpose, Device offers an option which is called a global shutter that can be used to turn on the light on the photodetector. Therefore, the transient simulation starts under dark condition; then the global source shutter is used to turn on the light after a particular time.

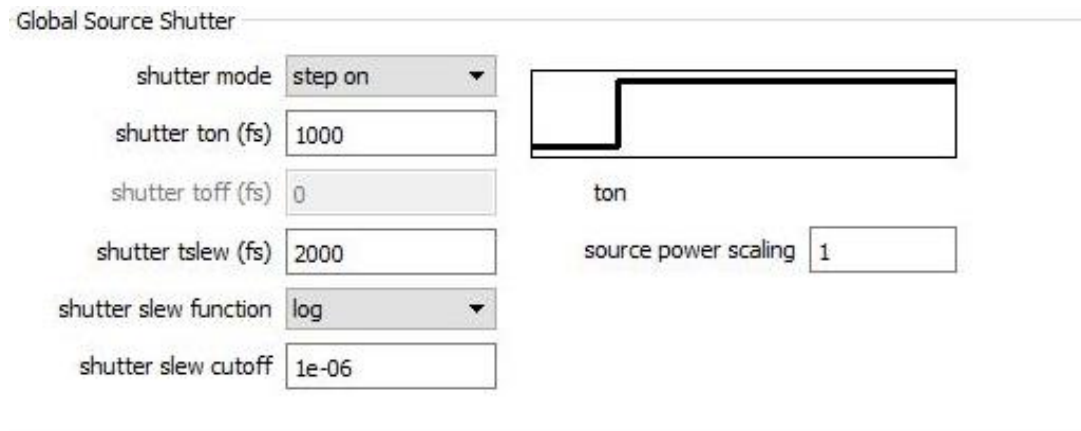


Figure 3.12 Global source shutter window on Device

Shutter mode can be chosen as step on-off, pulse on-off and disabled for not applying the generation rate. Shutter ton sets the on time for shutter while the toff is doing the opposite. Shutter tslew sets slew for the shutter. Shutter slew function allows the user to choose the transition function between the on and off states. In the Shutter slew cutoff, shutter uses the logarithmic function to step from the mentioned value to 1 to turn it on

and from 1 to the indicated value to turn it off. Source power scaling can be used to scale the amplitude of the source. By using global source shutter, now one can start the transient simulation under the dark condition and turn on the light on certain time to record the change of the photocurrent in the device. Now, it is possible to name the response of the photocurrent as the step response of the device's system. The impulse response of the device can be calculated by applying derivation on the step response which is going to lead to finding the 3dB cutoff frequency. [13]

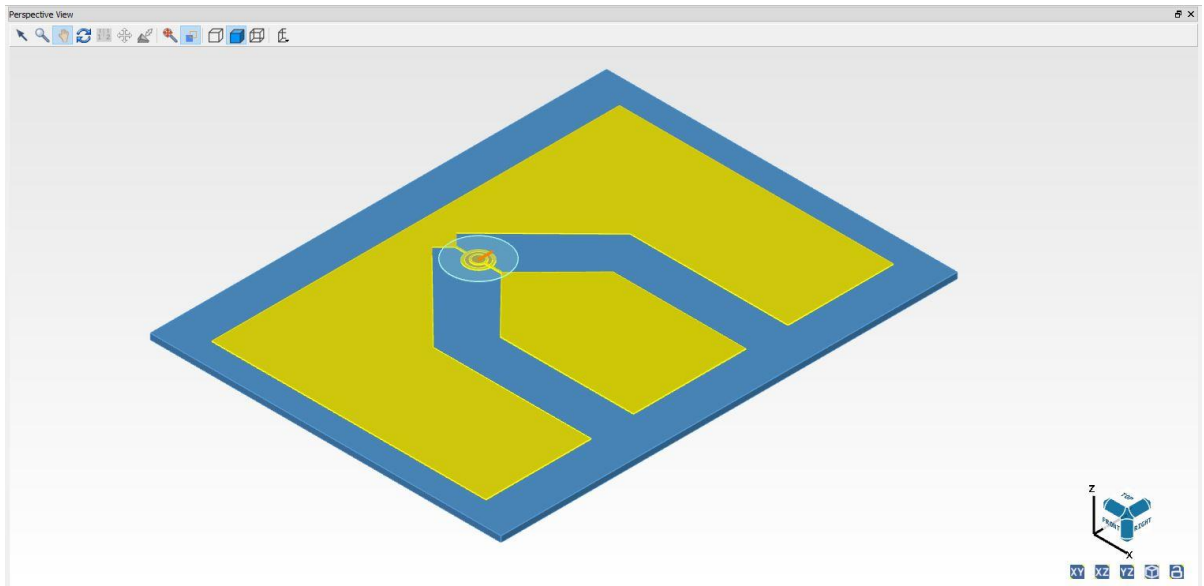


Figure 3.13 Perspective view of the UTC-PD in Device

Figure 3.13 shows the general view of the UTC-PD in Device software. Contacts metal are Au. The user can manipulate the directions by dragging the geometric object or clicking the navigation panel on the right side of the page.

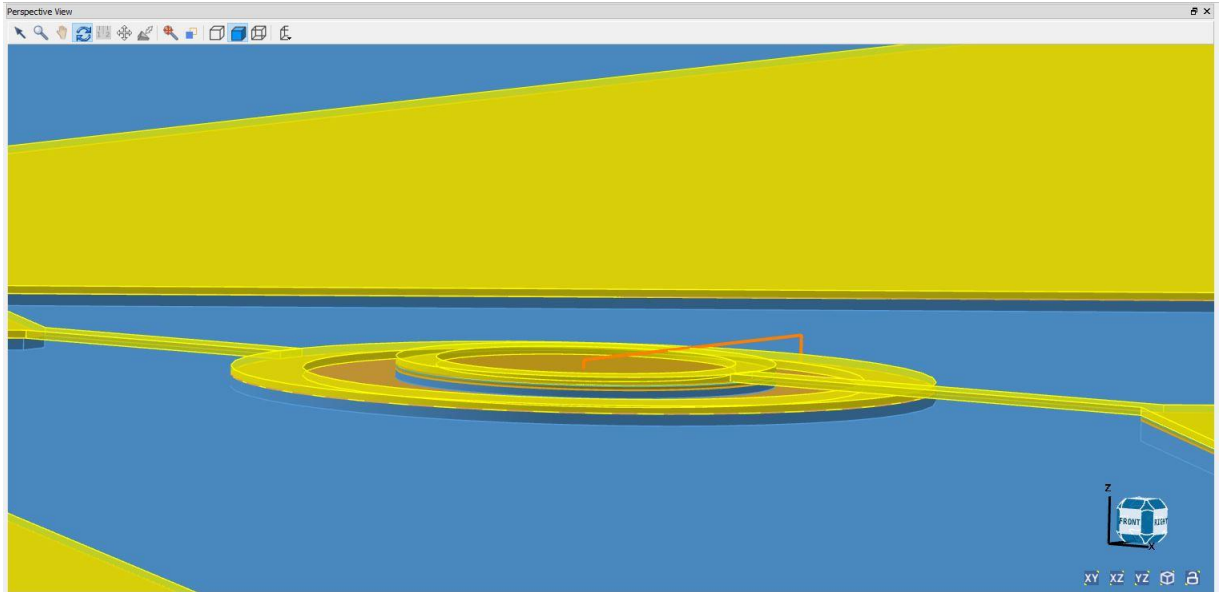


Figure 3.14 Perspective view of an active region in Device

Figure 3.14 illustrates the perspective view of the active region of the device. In the chapter, details of the layers in the device are given. There are also some options that can be seen on the top of the view window such as hidden line, wireframe etc.

## Chapter 4

### DESCRIPTION OF THE SIMULATION MODEL AND RESULTS

In this chapter, the details of the device are given for each layer. Also, the results about the simulation such as responsivity, current-voltage relation, and bandwidth are presented.

#### 4.1 Simulation model's description

In this section, the details of the epitaxial layers are given both for GaAsSb UTC-PD and InGaAs UTC-PD. In Table 4.1, for GaAsSb/InP UTC-PD, GaAsSb is used as a p-contact layer and as an absorption layer in the structure. The absorption layer is divided into two separate layers. The first absorption layer is 800 Å and p-doped while the second one is thinner with 200 Å and p-doped again. 200 Å GaAsSb layer is also used for the p-contact layer with p-doping. For the diffusion blocking layer, AlGaAsSb is preferred with 200 Å and p-typed. For the collector and sub-collector layers, InP is selected with 2000 Å and 3000 Å respectively with n-type doping. Lastly, 100 Å InGaAs layer is used as an etch-stop layer. It should be noted that the photodetector is top illuminated.

Table 4.1 Epitaxial layers of GaAsSb UTC-PD

Epitaxial Layers	Thickness(Å)	Doping levels (cm <sup>-3</sup> )	Comments
GaAs <sub>0.51</sub> Sb <sub>0.49</sub>	200	5×10 <sup>19</sup> p-type	p-contact layer
Al <sub>0.2</sub> Ga <sub>0.8</sub> As <sub>0.51</sub> Sb <sub>0.49</sub>	200	6×10 <sup>19</sup> p-type	Diffusion block layer
GaAsSb	800	5.6×10 <sup>17</sup> p-type	Absorption layer
GaAsSb	200	2×10 <sup>17</sup> p-type	Absorption layer
InP	2000	3×10 <sup>16</sup> n-type	Collector layer
InGaAs	100	1×10 <sup>19</sup> n-type	Etch-stop layer
InP	3000	3×10 <sup>19</sup> n-type	InP-subcollectors
InP semi-insulating substrate			

This project aims to compare the two competitive materials for their performance on UTC-PD as absorption layers. To achieve this purpose, the absorption layers that are made of GaAsSb in the UTC-PD are replaced with InGaAs. In Table 4.2, in the simulation of InGaAs/InP UTC-PD, InGaAs is used as p-contact, an absorption layer, and etch-stop layer. AlGaAsSb is chosen as 200 Å diffusion block layer with p-type doping while InP is preferred as collector and sub-collector layers again with Table 4.2 Epitaxial layers of InGaAs UTC-PD with 2000 Å and 3000 Å respectively with n-type doping. Both in GaAsSb and InGaAs UTC-PD simulations, 2000 Å Au is used as an electrical contact.

Table 4.2 Epitaxial layers of InGaAs UTC-PD

Epitaxial Layers	Thickness(Å)	Doping levels (cm <sup>-3</sup> )	Comments
InGa <sub>0.53</sub> As <sub>0.47</sub>	200	5×10 <sup>19</sup> p-type	p-contact layer
Al <sub>0.2</sub> Ga <sub>0.8</sub> As <sub>0.51</sub> Sb <sub>0.49</sub>	200	6×10 <sup>19</sup> p-type	Diffusion block layer
InGa <sub>0.53</sub> As <sub>0.47</sub>	800	5.6×10 <sup>17</sup> p-type	Absorption layer
InGa <sub>0.53</sub> As <sub>0.47</sub>	200	2×10 <sup>17</sup> p-type	Absorption layer
InP	2000	3×10 <sup>16</sup> n-type	Collector layer
InGaAs	100	1×10 <sup>19</sup> n-type	Etch-stop layer
InP	3000	3×10 <sup>19</sup> n-type	InP-subcollectors
InP semi-insulating substrate			

#### 4.2 Results for GaAsSb/InP UTC-PD

In this section results such as IV curve, responsivity and frequency response in both 1.3 and 1.55 μm wavelengths are given for GaAsSb/InP UTC-PD. For both dark and illuminated cases, anode voltage swept from -5V to 1.5V. Figure 4.1 and Figure 4.2 shows the relation between the current and biased voltage for with an absence of light and illumination which is a 1mW light source for 1.3 μm and Figure 4.2 for 1.55 μm respectively.

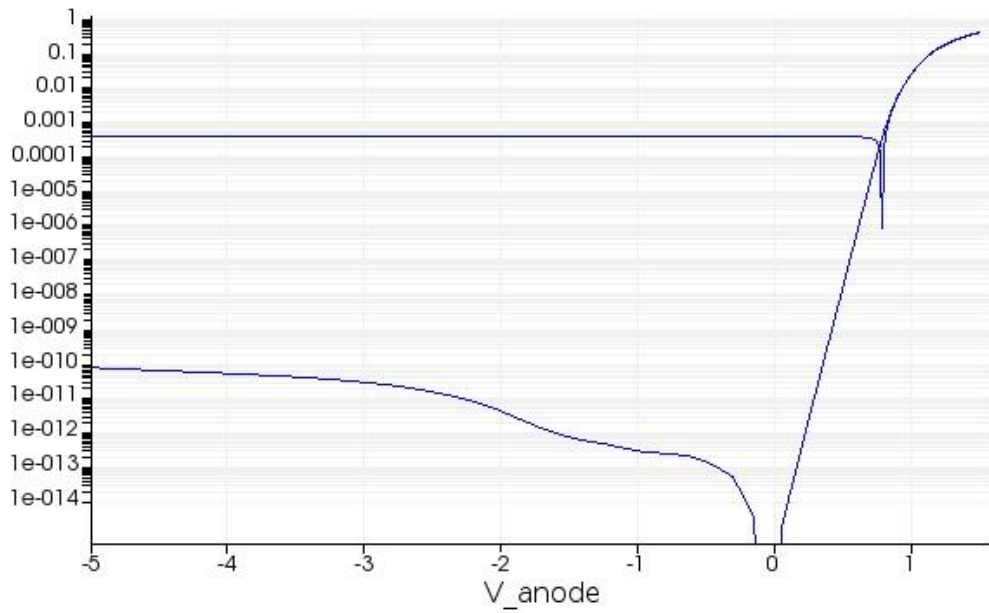


Figure 4.1 Current-Voltage relation of GaAsSb/InP UTC-PD under dark and 1mW illumination for 1.3  $\mu\text{m}$

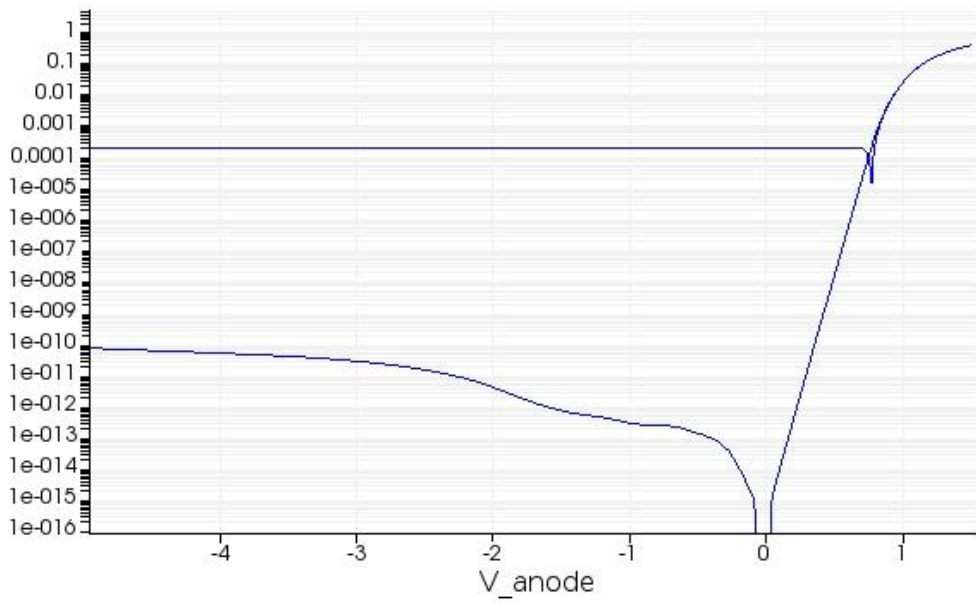


Figure 4.2 Current-Voltage relation of GaAsSb/InP UTC-PD under dark and 1mW illumination for 1.55  $\mu\text{m}$

As it can be observed from the Figure 4.1 and Figure 4.2, even the device is not exposed to light; there is still a very small amount of dark current due to the thermal generation of electron-hole pairs. It also should be noted that under illumination, the reverse current reaches its saturation level even for small reverse bias voltage. To obtain the dark current, generation rate needs to be disabled. GaAsSb is absorbing more power from the light source in 1.3  $\mu\text{m}$  when it is compared to situation in 1.55  $\mu\text{m}$ . This leads to obtaining higher photocurrent under reverse bias in 1.3  $\mu\text{m}$ .

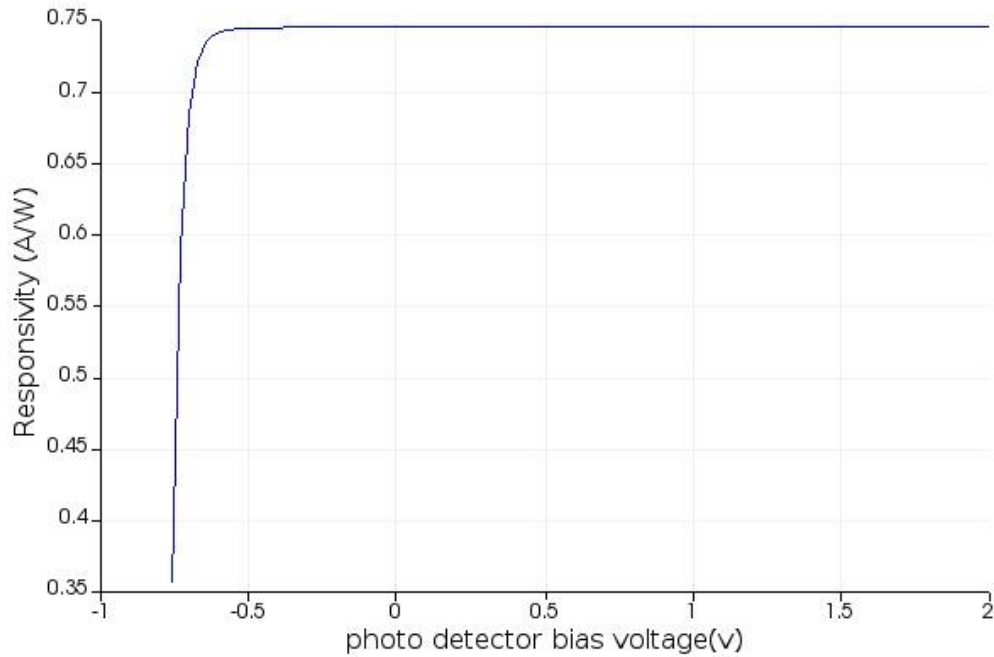


Figure 4.3 Responsivity (A/W) in 1.3  $\mu\text{m}$  wavelength for GaAsSb/InP UTC-PD

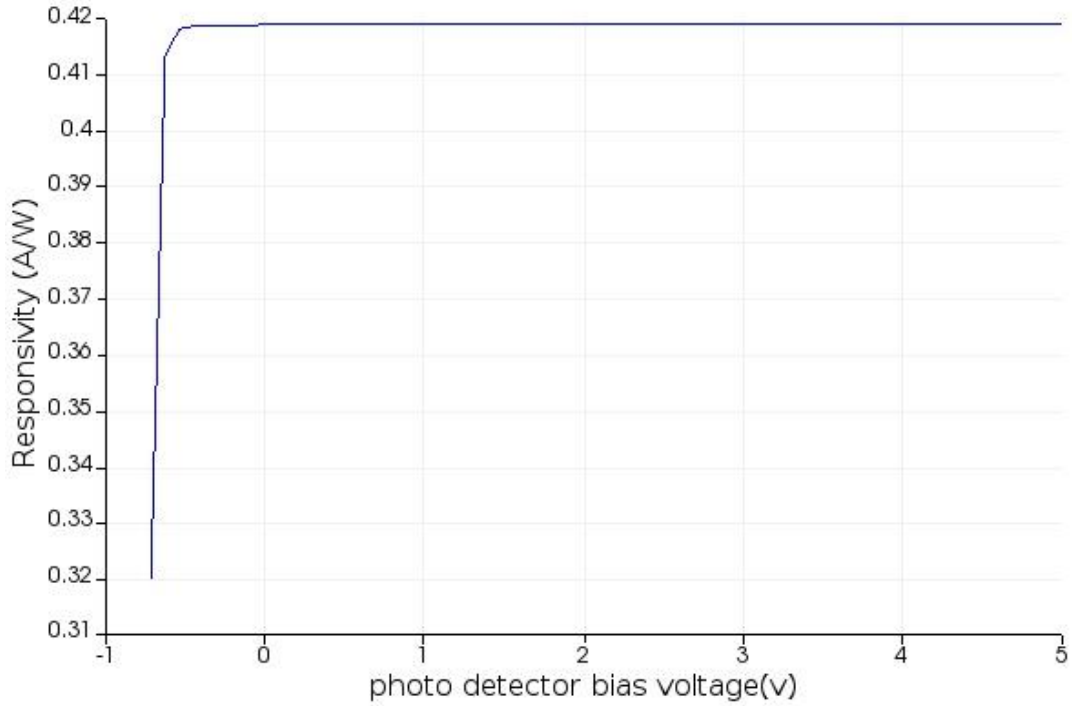


Figure 4.4 Responsivity (A/W) in 1.55  $\mu\text{m}$  wavelength for GaAsSb/InP UTC-PD

Figure 4.2 illustrates the responsivity of the device for a 1.3  $\mu\text{m}$  wavelength while Figure 4 Responsivity is described as the sensitivity of the device to the exposed light. In other words, it is the ratio of the photocurrent  $I_p$  to the incident light power which shows how efficient is converting the optical power to the electrical current. This relation is given in Equation 4.1, [24]

$$R_\lambda = \frac{I_p}{P} \quad (4.1)$$

To find the responsivity (steady-state simulation), in Device software, generation rate is enabled and set to 0.001 which corresponds to 1mW optical power. It needs to be highlighted that allowing the generation rate basically means illuminating the device. In this scheme, the Device software starts to consider the electron-hole pairs that are

generated due to the illumination. Then simulation is run by biasing the contacts from 0.75 to -2 volts to find out how responsivity is changing with applied bias. In -2 volts, the responsivity is obtained as 0.74 A/W. Gaining a higher amount of the current in 1.3  $\mu\text{m}$  enables to get higher responsivity in the corresponding wavelength.

Current optical communication systems require high bandwidth to be able to transmit big and high-speed data. Therefore, all the electronic, optic and optoelectronic devices need to cope with the increasing trend. In this case, photodetector also must be able to work with high-frequency data precisely. The transient time of the photogenerated carriers plays a critical role to determine the bandwidth of the photodetector. [13], [23]

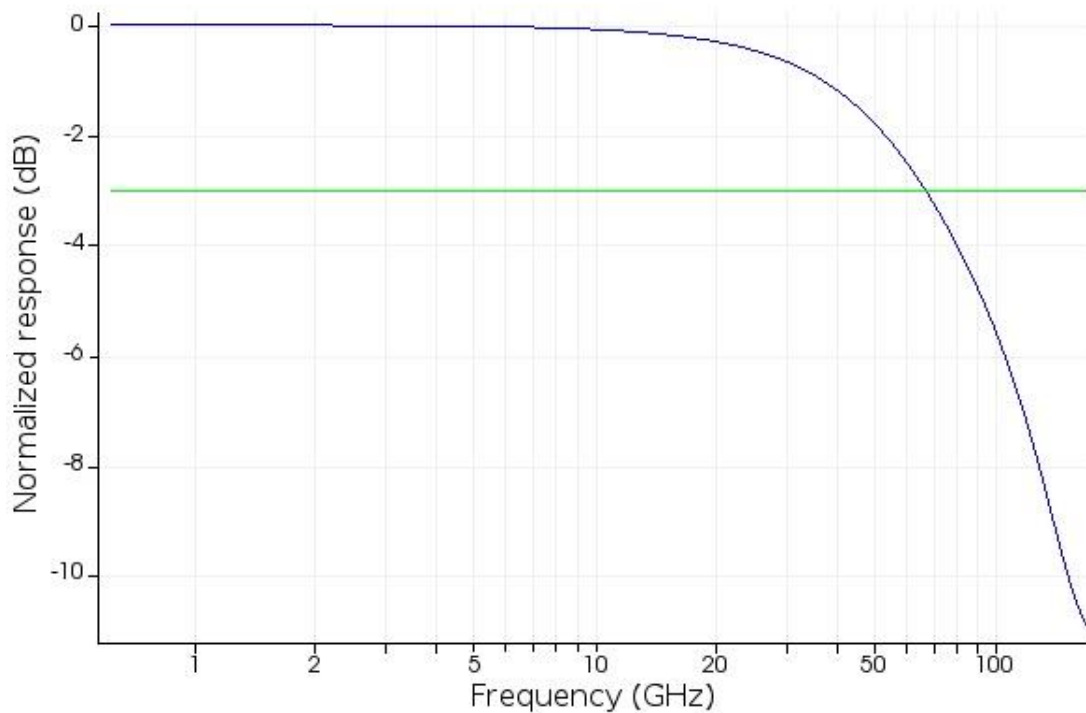


Figure 4.5 3 dB cutoff frequency in 1.3  $\mu\text{m}$  wavelength for GaAsSb/InP UTC-PD  
 $f_{3dB} = 66.4 \text{ GHz}$

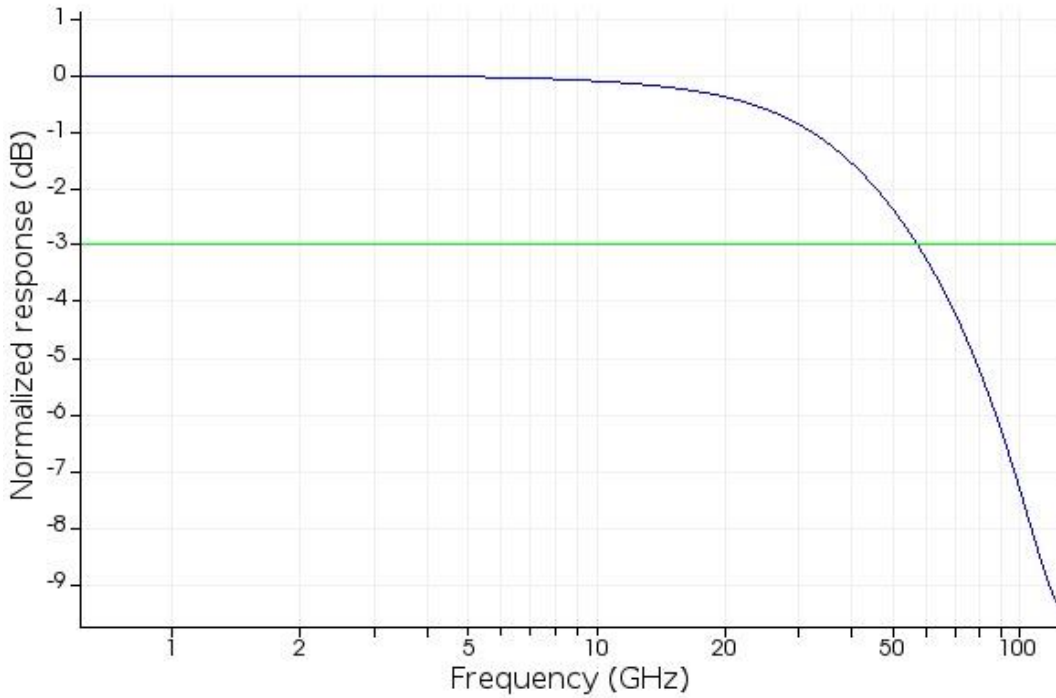


Figure 4.6 3 dB cutoff frequency for GaAsSb in 1.55  $\mu\text{m}$  wavelength for GaAsSb/InP UTC-PD  $f_{3dB} = 56.9 \text{ GHz}$

To find out the 3-dB cut-off frequency for the UTC-PD, transient simulation is done in DEVICE by switching the solver to transient mode. All the contacts are set to be time dependent. The cathode voltage is set to be fixed; however, regarding being time-dependent, solver applies the same fixed voltage at every time step. There are two-time points for anode contacts which are 0 ps and 1ns. For these points the voltage is set to -0.5 V. Minimum time step is 200 fs. Shuttering is set for a step on function. The turn-on time of 1 ps and a slew of 2 ps. [13]

### 4.3 Results for InGaAs/InP UTC-PD

In this part, the results for InGaAs-InP UTC-PD such as IV curve, responsivity and frequency response in both 1.3 and 1.55  $\mu\text{m}$  wavelengths are given. For both dark

and illuminated cases, anode voltage swept from -5V to 1.5V. Figure 4.7 and Figure 4.8 illustrate the relation between the current and biased voltage for under illumination and dark condition. Illumination power is a 1mW light source for 1.3  $\mu\text{m}$  and for 1.55  $\mu\text{m}$  respectively.

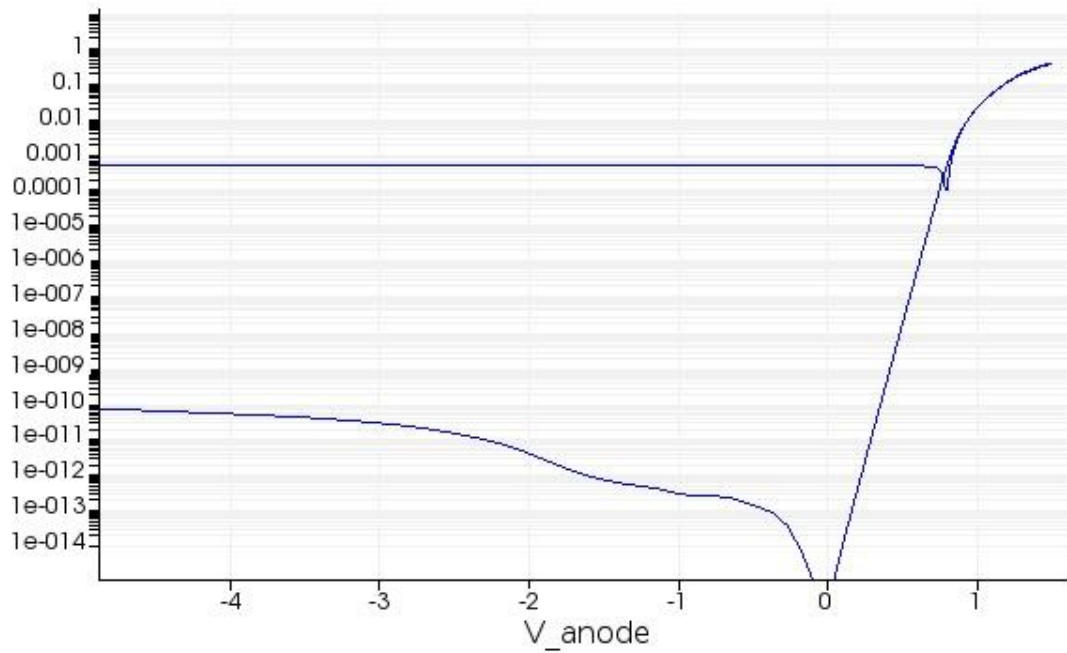


Figure 4.7 IV curve for under dark and illumination for InGaAs/InP UTC-PD for 1.3  $\mu\text{m}$

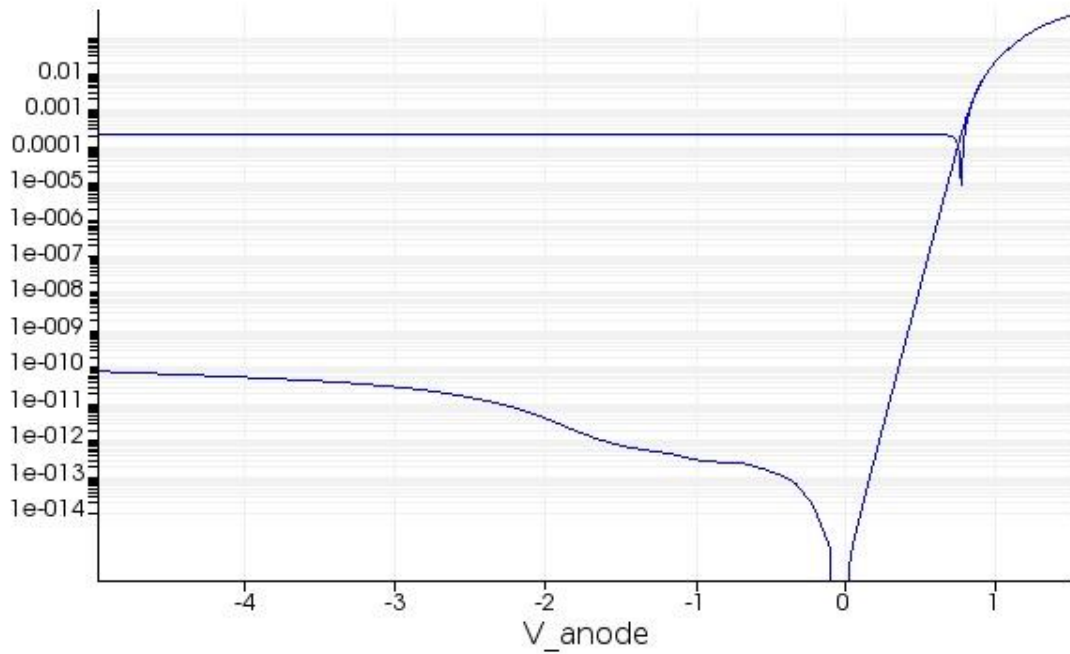


Figure 4.8 IV curve for under dark and illumination for InGaAs/InP UTC-PD for 1.55  $\mu\text{m}$

As can be observed from Figure 4.7 and Figure 4.8 illuminated current under reverse bias is higher in 1.3  $\mu\text{m}$  when it is compared to 1.55  $\mu\text{m}$ . Both GaAsSb and InGaAs are showing higher level current for 1.3  $\mu\text{m}$ .

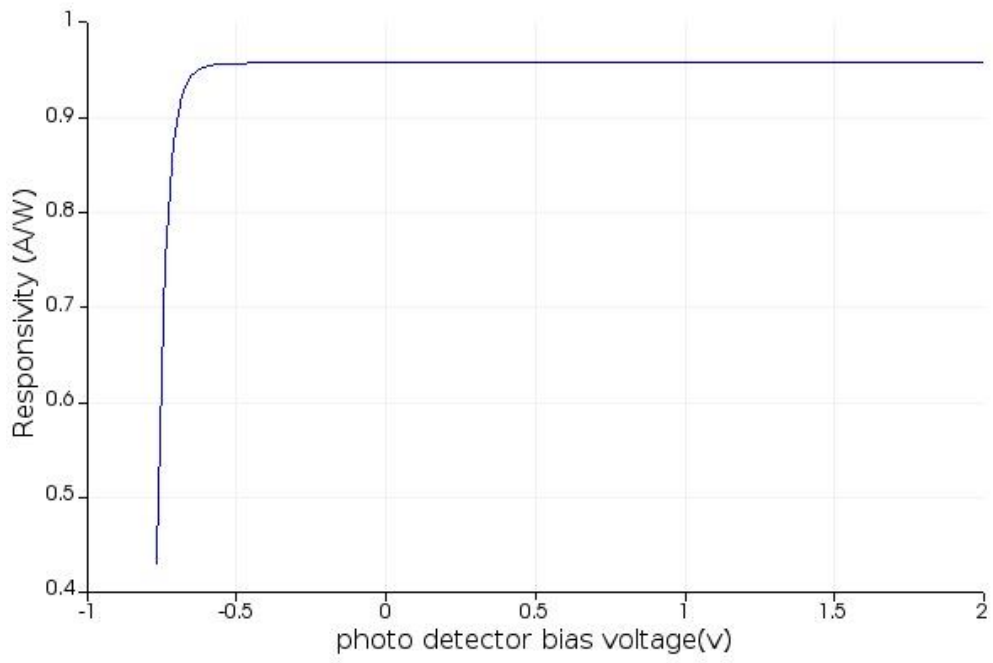


Figure 4.9 Responsivity for InGaAs/InP UTC-PD for 1.3 μm

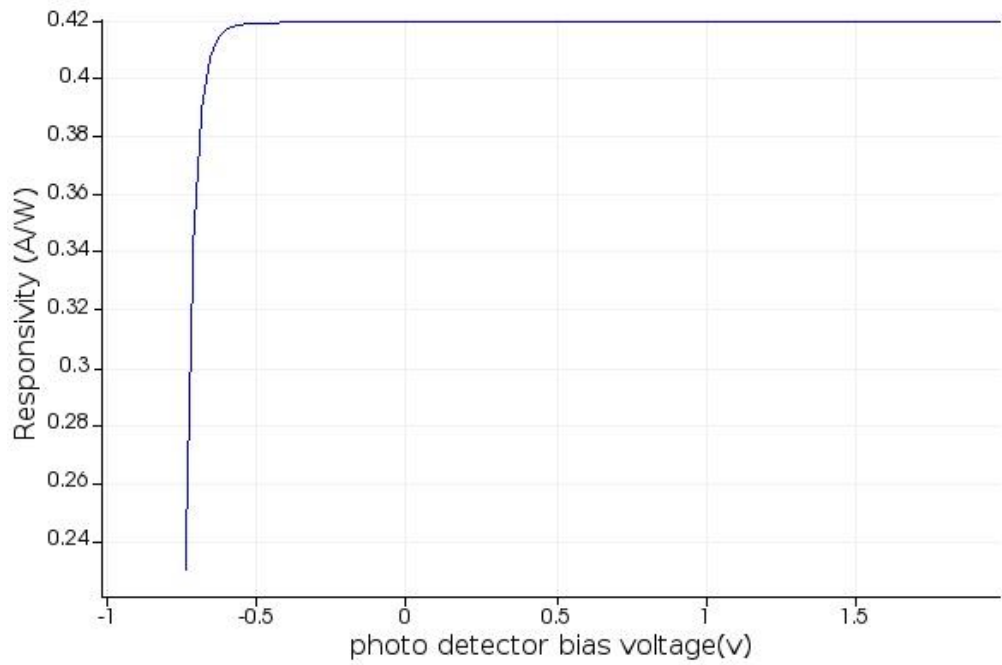


Figure 4.10 Responsivity for InGaAs/InP UTC-PD for 1.55 μm

Another important point is that InGaAs/InP UTC-PD is experiencing the same situation with GaAsSb/InP UTC-PD which is even for a small amount of applied reverse bias voltage, current saturates rapidly. Regarding responsivity, Figure 4.9 shows the responsivity as 0.94 A/W for 1.3  $\mu\text{m}$  while Figure 4.10 shows the responsivity as 0.42 A/W for 1.55  $\mu\text{m}$ . In conclusion, GaAsSb/InP UTC-PD with 100 nm thickness absorption layer, shows 3 dB bandwidth 66.4 GHz for 1.3  $\mu\text{m}$  and 46.9 GHz for 1.55  $\mu\text{m}$  wavelengths. The reason behind this is that the electrons travel faster in 1.3  $\mu\text{m}$  wavelength which causes obtaining higher bandwidth. As mentioned before, for all the simulation cases, the same optical input power (1 mW) is used. When the the same amount of power is used, the number of photons arrived at the photodetector is comparatively lower in 1.3  $\mu\text{m}$  wavelength. As a result of this, in 1.55  $\mu\text{m}$  wavelength, photogenerated carriers are less than the 1.3  $\mu\text{m}$  wavelength for the same material. This causes less electric field in the 1.55  $\mu\text{m}$ . Since the electric field sweep the electrons, higher electric field triggers to observe faster travel time which results in higher bandwidth in 1.3  $\mu\text{m}$ . Having high responsivity and high bandwidth such as 0.74 A/W, 66.4 GHz for 1.3  $\mu\text{m}$  and 0.42 A/W, 46.9 GHz for 1.55  $\mu\text{m}$  respectively, indicates that the GaAsSb/InP UTC-PD is able to respond to high-speed signals with high efficiency. InGaAs/InP UTC-PD has a responsivity of 0.94 A/W for 1.3  $\mu\text{m}$  wavelength and 0.42 A/W for 1.55  $\mu\text{m}$  wavelength. These numbers make InGaAs/InP UTC-PD more efficient than GaAsSb/InP for 1.3  $\mu\text{m}$  wavelength. However, since the memory requirements for the transient simulation of InGaAs structure exceeds the current system that the author can access, the frequency response could not be obtained. Therefore, the comparison between these two candidate materials for frequency response is not complete.

## REFERENCES

1. Liguang, Z., Xiong, Z., Yuping, Z., Tatavarti, S. R., Watkins, S. P., Bolognesi, C. R., Demiguel, S., ... OFC/NFOEC 2008. 2008 Optical Fiber Communication Conference/National Fiber Optic Engineers Conference. (March 01, 2005). Demonstration of high-speed staggered lineup GaAsSb-InP untraveling carrier photodiodes. *Ieee Photonics Technology Letters*, 17, 3, 651-653.
2. Topical Meeting on Ultrafast Electronics and Optoelectronics, Nuss, M., Bowers, J. E., & Optical Society of America. (1997). Ultrafast electronics and optoelectronics: From the topical meeting, Ultrafast Electronics and Optoelectronics, March 17-19, 1997, Incline Village, Nevada. Washington, DC: Optical Society of America.
3. Srivastava, S., & Roenker, K. P. (January 01, 2004). Numerical modeling study of the InP/InGaAs uni-travelling carrier photodiode. *Solid State Electronics*, 48, 3, 461-470.
4. Nagatsuma, T., Ito, H., & Ishibashi, T. (February 01, 2009). High-power RF photodiodes and their applications. *Laser & Photonics Reviews*, 3, 123-137.
5. Tadao Nagatsuma and Hiroshi Ito (March 22nd 2011). High-Power RF Uni-Traveling-Carrier Photodiodes (UTC-PDs) and Their Applications, *Advances in Photodiodes*, Gian Franco Dalla Betta, IntechOpen, DOI: 10.5772/14800. Available from: <https://www.intechopen.com/books/advances-in-photodiodes/high-power-rf-uni-traveling-carrier-photodiodes-utc-pds-and-their-applications>
6. Shrestha, Y. R. (2005). Numerical simulation of GaAsSb/InP uni-traveling carrier photodiode (UTC-PD). Cincinnati, Ohio: University of Cincinnati.
7. Li, W. (2014). InGaAs/InP modified uni-travelling-carrier photodiode with a cliff layer.
8. Nabet, B. (2015). Photodetectors: materials, devices and applications in communications and imaging technologies. Retrieved from <https://ebookcentral.proquest.com>

9. Nagatsuma, T., Kaino, A., Hisatake, S., Ajito, K., Song, H., Wakatsuki, A., . . . Kado, Y. (2010). Continuous-wave Terahertz Spectroscopy System Based on Photodiodes. *PIERS Online*, 6(4), 390-394. doi:10.2529/piers091029132808
10. Wai, L. C., Jason, D., & Daniel, M. M. (August 01, 2007). Imaging with terahertz radiation. *Reports on Progress in Physics*, 70, 8, 1325-1379.
11. Nagatsuma, T., Kumashiro, T., Fujimoto, Y., Taniguchi, K., Ajito, K., Kukutsu, N., . . . Kado, Y. (2009). Millimeter-wave imaging using photonics-based noise source. 2009 34th International Conference on Infrared, Millimeter, and Terahertz Waves. doi:10.1109/icimw.2009.5325747
12. Blum, O., Fritz, I. J., Dawson, L. R., Howard, A. J., Headley, T. J., Klem, J. F., & Drummond, T. J. (1995). Highly reflective, long wavelength AlAsSb/GaAsSb distributed Bragg reflector grown by molecular beam epitaxy on InP substrates. *Applied Physics Letters*, 66(3), 329-331. doi:10.1063/1.114202/
13. High-Performance Nanophotonic Simulation Software. (n.d.). Retrieved January 3, 2019, from <https://www.lumerical.com>
14. University of Reading. (n.d.). Accessibility navigation. Retrieved from <http://www.reading.ac.uk/ir-substrateopticaltheory-absorptionandextinctioncoefficienttheory.aspx>
15. Gupta, M. C. (1997). *The handbook of photonics*. Boca Raton, Fla: CRC Press.
16. RefractiveIndex.INFO. (n.d.). Retrieved from <https://refractiveindex.info/>
17. Park, M. S., & Jang, J. H. (January 01, 2008). GaAs<sub>0.5</sub>Sb<sub>0.5</sub> lattice matched to InP for 1.55 mm photo-detection. *Electronics Letters*, 44, 8, 549.
18. Adachi, S. (1992). *Physical properties of III-V semiconductor compounds: InP, InAs, GaAs, GaP, InGaAs, and InGaAsP*. New York: Wiley.
19. Menon, P. S., Zhang, X., Ming, H., Kandiah, K., Ehsan, A. A., Chen, M. Y., Shaari, S., ... Photonics Asia 2007. (November 29, 2007). An interdigitated diffusion-based In<sub>0.53</sub>Ga<sub>0.47</sub>As lateral PIN photodiode.
20. Rumyantsev, S. L., Shur, M., & Levinshtein, M. E. (1999). *Handbook series on semiconductor parameters: Vol. 2*. Singapore, London: World Scientific.
21. Humphreys, D., King, R., Jenkins, D., & Moseley, A. (1985). Measurement of absorption coefficients of Ga<sub>0.47</sub>In<sub>0.53</sub>As over the wavelength range 1.0–1.7 μm. *Electronics Letters*, 21(25-26), 1187. doi:10.1049/el:19850839

22. Nee, T. W., & Green, A. K. (November 15, 1990). Optical properties of InGaAs lattice-matched to InP. *Journal of Applied Physics*, 68, 10, 5314-5317.
23. Shrestha, Y. R. (2005). Numerical simulation of GaAsSb/InP uni-traveling carrier photodiode (UTC-PD). Cincinnati, Ohio: University of Cincinnati.
24. OSI optoelectronics. *Photodiode characteristics and applications* [PDF File]. Retrieved from <http://www.osioptoelectronics.com/application-notes/AN-Photodiode-Parameters-and-Characteristics.pdf>